

Producing slow light in warm alkali vapor using electromagnetically induced transparency

Kenneth DeRose, Kefeng Jiang, Jianqiao Li, Linzhao Zhuo, Hong Cai, and S. Bali*

Department of Physics, Miami University, Oxford, Ohio 45056-1866, USA

*Corresponding author: balis@miamioh.edu

Compiled March 18, 2022

We present undergraduate-friendly instructions on how to produce light pulses propagating through warm Rubidium vapor with speeds less than 400 m/s, i.e., nearly a million times slower than c . We elucidate the role played by electromagnetically induced transparency (EIT) in producing slow light pulses, and discuss how to achieve the required experimental conditions. Various EIT linewidth broadening mechanisms are described. The optical set up is presented, and details provided for preparation of pump, probe, and reference pulses of required size, intensity, temporal width, and polarization purity. We discuss in detail how to adequately magnetically shield the alkali vapor sample. Our instructions include drawings for parts and information on prices and vendors. In the spirit of presenting a stand-alone article for producing slow light, we provide in Supplementary Notes, a detailed semiclassical derivation of EIT and slow light that should be amenable to advanced undergraduates, and details of an auxiliary measurement to ensure the suppression of residual stray magnetic fields below 0.2 milliGauss over the entire laser-atom interaction region.

© 2022 Optical Society of America

1. Introduction

It has been two decades since the first demonstration of slow optical pulses propagating through atomic media [1, 2]. Slow light was revealed as a striking consequence of a quantum mechanical phenomenon in light-matter interaction known as EIT, i.e., electromagnetically induced transparency. EIT arises from the interference between probability amplitudes for absorption pathways which are simultaneously excited by two resonant light fields - one strong, referred to as the pump (or coupling) field, and the other weak, referred to as the probe [3, 4]. EIT and slow light in warm alkali vapor continue to be intensely researched topics in quantum information and quantum technology, particularly in the context of robust quantum memories [5–7], and stable photon-shot-noise-limited electromagnetic field sensors using Rydberg atoms [8]. In Ref. [6], for instance, the authors provide an overview of current approaches to quantum memory, stating that “...although all of these approaches have been studied and demonstrated, EIT remains the most popular scheme for quantum memory” [because] “in comparison to the other approaches, the EIT approach has a long storage time and is a relatively easy-to-implement and inexpensive solution”.

An excellent article on EIT-based experiments for undergraduate laboratories was published just over a decade ago [9]. Elegant EIT-based experiments carried out at undergraduate institutions have also been reported [10]. However, an undergraduate-friendly *experimental description of slow light* in atomic vapor does not exist. In this paper we endeavor to fill this gap. This is important because an increasing number of physics and engineering majors wish to get involved in the development of cutting-edge quantum technologies. There are several pedagogical advantages to introducing the concepts of EIT and slow light in an optics class

for undergraduate seniors and first/second-year graduate students. For instance, in the advanced lecture/lab course “Optics and Laser Physics” that we teach at [name removed for reviewing purposes], students often ask, “We’ve read about laser applications in imaging and communications and medicine...can you tell us about *quantum* applications we haven’t heard of?”

EIT and slow light can provide a satisfactorily impactful answer, on the theoretical as well as experimental front. On the theory side EIT physics is a natural extension to what these students have already been learning about light-matter interaction. Early in the semester they are well-versed in setting up population-rate equations for a laser system, which also sets the stage for an EIT-based slow light system, since the simplest model for either system is provided by a three-level atom. The students are therefore primed to take the step up from simple population rates (diagonal elements of the probability density matrix $\hat{\rho}$ for light-atom interaction, where the caret denotes a quantum mechanical operator) to a more nuanced consideration of the coherences (off-diagonal elements of $\hat{\rho}$) in order to understand the quantum interference underlying EIT. Similarly, the students know already about group versus phase velocity, and therefore enjoy learning about how a steep positive gradient of the refractive index within a narrow EIT spectral window can lead to a dramatically slow group velocity.

On the experimental side, the class is divided into four groups of two or three students each. The advanced lab component of the course culminates in each student group constructing an external cavity-tunable diode laser system and performing saturated absorption spectroscopy [11–13]. Interested students may extend their advanced lab experience, in the form of an independent study for a semester or two, and carry out the experiments on EIT and slow light described in this paper.

Below we first present basic theory for EIT and slow light. Calculation details, starting with the Schrödinger equation, are provided in Sec. 1 of the Supplementary Notes [14]. Next, we describe our experimental set up for producing slow light pulses. Details for suppression of stray magnetic fields in the laser-atom interaction region are provided in Secs. 2 and 3 of Ref. [14]. Finally, we present our data and discuss our experimental results.

2. Theory

The theoretical discussion of EIT and slow light centers around calculating the complex refractive index $n = n_r + i n_i$ of the medium. The imaginary part n_i yields the absorption spectrum α where EIT in atomic media is revealed as a narrow transparency window near resonance. The real part n_r yields the group velocity v_g of light propagating through the medium. Slow light is revealed as a consequence of the steep frequency-variation of n_r within the EIT transparency window.

The theory behind EIT and slow light has been explained in several high-quality undergraduate-friendly articles (see, for example, Refs. [9, 15–17]), but is typically taught in quantum optics or atomic physics classes at the graduate level - for an excellent graduate student level treatment see Ref. [1]. In the spirit of presenting a complete stand-alone reference we provide in Sec. 1 of the Supplementary Notes [14] a detailed description which is amenable to advanced juniors and seniors: There we show how to calculate n_r and n_i and reveal the basic physics behind EIT and slow light. Here, we note just the main results.

Following the notation in Ref. [1] we depict a fictitious three-level atomic model in Fig. S1, in which transitions are allowed between states 1 and 3 and between states 2 and 3 but not between states 1 and 2. The standard

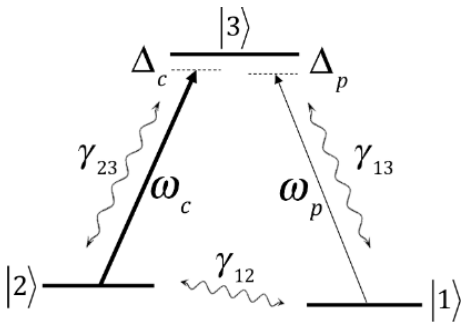


Fig. 1. Three-level atomic model. A strong coupling (or pump) beam of frequency ω_c and a weak probe beam of frequency ω_p , are both tuned to near-resonance with $|3\rangle$ from levels $|2\rangle$ and $|1\rangle$ respectively, with detunings Δ_c and Δ_p . Decoherence rates between levels 3 and 1, 3 and 2, 2 and 1, are denoted by γ_{13} , γ_{23} , γ_{12} , respectively.

EIT experiment consists of a strong coupling (or pump) beam of frequency ω_c and a weak probe beam of frequency ω_p , both tuned to near-resonance with $|3\rangle$ from levels $|2\rangle$ and $|1\rangle$ respectively, with detunings Δ_c and

Δ_p . We assume that the pump beam only addresses the coupling transition $|2\rangle \rightarrow |3\rangle$ and the probe beam only addresses the $|1\rangle \rightarrow |3\rangle$ transition. The probe frequency is scanned around the (fixed) pump frequency, and the probe transmission spectrum is measured.

We start with the Hamiltonian and the Schrödinger equation for the three-level system in Fig. S1(a), and derive the widely used optical Bloch equations. These equations describe the time-evolution of the matrix elements of the probability density matrix ρ , from which we calculate the complex refractive index n of the gaseous sample. Using the the well-known relation between the absorption coefficient α and the imaginary refractive index n_i [14]: $\alpha = 2n_i\omega/c$, we find for α (please see Sec. 1 in Ref. [14] for the complete calculation and explanation):

$$\alpha = \frac{N\omega_p |\mu_{13}|^2}{\epsilon_0 c \hbar} \quad (1)$$

$$\times \frac{\gamma_{13}\Delta'^2 + \gamma_{12}(\gamma_{12}\gamma_{13} + |\chi_c|^2)}{[\Delta_p\Delta' - \gamma_{12}\gamma_{13} - |\chi_c|^2]^2 + [\gamma_{12}\Delta_p + \gamma_{13}\Delta']^2}$$

and for the real part of the refractive index n_r

$$n_r = 1 + \frac{N}{2\epsilon_0} \frac{|\mu_{13}|^2}{\hbar} \quad (2)$$

$$\times \frac{\Delta'(\Delta'\Delta_p - |\chi_c|^2) + \gamma_{12}^2\Delta_p}{[\Delta_p\Delta' - \gamma_{12}\gamma_{13} - |\chi_c|^2]^2 + [\gamma_{12}\Delta_p + \gamma_{13}\Delta']^2}$$

where N is the number of atomic dipoles per unit volume, $\Delta' \equiv$ relative probe-coupling detuning $\Delta_p - \Delta_c$ (also referred to as the Raman detuning), $|\mu_{13}|^2$ is directly related to the Clebsch-Gordan coefficient for the probe transition, and χ_c is the coupling beam Rabi frequency defined as $\chi_c \equiv \vec{d}_{32} \cdot \vec{e}_c E_c / 2\hbar$ (see Sec. 1 in Ref. [14] for detailed explanations; \vec{d}_{32} is the transition dipole moment between levels $|2\rangle$ and $|3\rangle$, \vec{e}_c is the polarization of the coupling electric field; the coupling and probe beams are assumed to be monochromatic plane waves of frequency ω_c and ω_p respectively; note that the Rabi frequency depends on the amplitude E_c of the coupling electric field).

The expressions for absorption α and real refractive index n_r in Eqns. 27 and 28, are depicted in Figs. S2(a) and (b), respectively. EIT manifests as a dramatic drop in absorption when the coupling and probe beams are in resonance with each other. The following simplified approximate expressions for the EIT linewidth Γ_{EIT} and contrast Δa (or amplitude of the transparency window) can be extracted from Eqns. 27 and 28 [14]:

$$\Gamma_{EIT} = 2 \left(\gamma_{12} + \frac{|\chi_c|^2}{\gamma_{13}} \right) \quad (3)$$

$$\Delta a = \frac{|\chi_c|^2}{\gamma_{13}\gamma_{12} + |\chi_c|^2} \quad (4)$$

Direct inspection of Fig. S2(a) informs us that Eqn. 27 predicts a FWHM-linewidth of ~ 6 MHz for the EIT window, which is not too different from the prediction

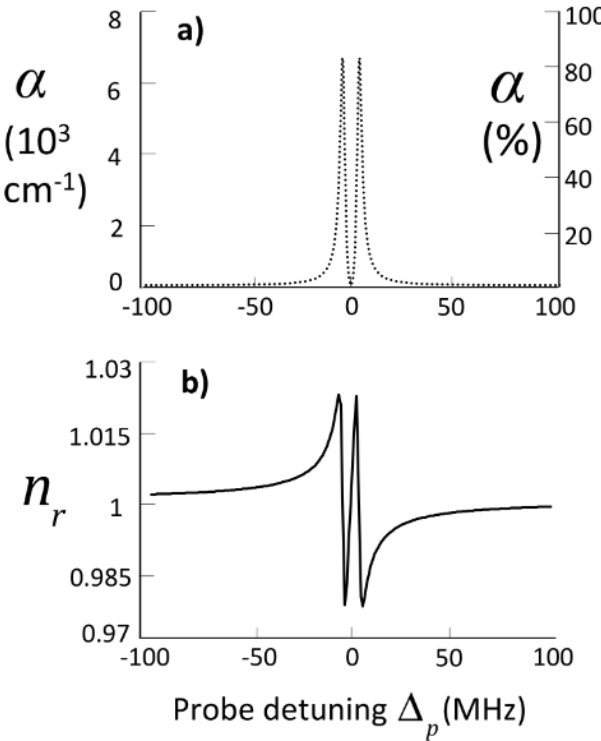


Fig. 2. The absorption coefficient α depicted in (a), and the real refractive index n_r in (b), as predicted by Eqns. 27 and 28. We used parameter-values close to our experimental conditions: $|\chi_c|/2\pi = 4 \text{ MHz}$, $\omega_p/2\pi = 3.77 \times 10^{14} \text{ Hz}$, $N = 3.36 \times 10^{11}/\text{cm}^3$, $|\mu_{13}| = 2.54 \times 10^{-29} \text{ Cm}$ [5], $\Delta_c = 0$. For the ^{87}Rb D1 transition $\gamma_{13}/2\pi = \frac{1}{2}(5.75 \text{ MHz})$ [5], and $\gamma_{12}/2\pi = 3 \text{ KHz}$ [24].

of $\sim 11 \text{ MHz}$ by the approximate expression in Eq. 32. The parameter-values used are specified in Fig. S2's caption, and are close to our experimental conditions. Nearly 100% transparency is predicted in Fig. S2(a) by Eqn. 27, in agreement with the approximate expression in Eqn. 33.

However, the theoretical predictions in Eqns. 27 - 33 for the EIT linewidth and contrast yield unrealistic numbers. In order to understand why and also gain a physical understanding of the origin of the transparency window, we ask the question: What are the new eigenstates describing the three-level atomic system under illumination by the coupling and probe fields in Fig. S1? In Sec. 1 of the Supplementary Notes [14] we show that the atom is transferred to a “dark” state which is a quantum superposition of the two ground states $|1\rangle$ and $|2\rangle$. This dark state has no quantum overlap with the excited state $|3\rangle$, thus an atom once transferred to the dark state stays there.

In practice, though, the steady-state fraction of atoms settling in the dark state is significantly reduced. Our theory is based on a simple “closed three-level model” of a single stationary atom whereas the experiments use op-

tically dense samples of moving atoms with multi-levels. Thus there are extraneous energy-levels close by to which the population can leak. This leads to a severe reduction in measured EIT contrast. The lowered contrast implies that only the spectral components of the probe which lie at the center of the EIT transparency window can propagate through, causing a significant reduction in the observed linewidth [19]. Complicating matters further, there exist several additional EIT line-broadening mechanisms which are described in Sec. 3 B below.

Thus, the closed three-level expressions in Eqns. 27 - 33 above, while useful for visualizing the dependence of the EIT linewidth and contrast on various parameters as in Fig. S2, are not useful for making quantitative predictions of the linewidth and contrast actually observed in experiments. This important point is revisited in Sec. 6A when we discuss our data.

We shift focus now to the real refractive index n_r , plotted in Fig. S2(b) using Eqn. 28. Slow light arises from the dramatic change in refractive index n_r within the narrow EIT transparency window where the coupling (i.e., pump) and probe beams are in resonance with each other. This follows from the definition of the group velocity of light v_g which yields:

$$\frac{v_g}{c} \equiv \frac{1}{n_r + \omega_p d n_r / d \omega_p} \approx \frac{|\chi_c|^2}{|\chi_c|^2 + \frac{N|\mu_{13}|^2}{2\epsilon_0 \hbar} \omega_p} \quad (5)$$

In particular a steep *positive* gradient about zero detuning, as depicted in Fig. S2(b), leads to a significantly reduced group velocity. As explained in Sec. 1 of Ref. [14], the expression on the far right in Eqn. 43 is derived by setting $\Delta_c = 0$ for simplicity in Eqn. 28 and assuming that the coupling intensity is strong, i.e.,

$$|\chi_c|^2 \gg \Delta_p^2, \gamma_{12}^2, \gamma_{12}\gamma_{13}, |\Delta_p|\gamma_{13}. \quad (6)$$

If we choose the coupling intensity to also satisfy:

$$|\chi_c|^2 \ll \frac{N|\mu_{13}|^2}{2\epsilon_0 \hbar} \omega_p \quad (7)$$

we see from Eqn. 43 that $v_g/c \ll 1$, achieving slow light.

The conditions in Eqns. 41 and 44 are always satisfied in our experiments. To see how the strong intensity condition is satisfied, we draw upon the well-known connection between the Rabi frequency χ_c and intensity I [20,21]:

$$2\chi_c^2/\Gamma^2 \equiv I/I_{sat}, \quad \text{where } I_{sat} \equiv \frac{2\pi^2 \hbar c}{3\lambda^3} \Gamma \quad (8)$$

Here λ is the optical transition wavelength, and the saturation intensity I_{sat} for the transition [21] is defined as the excitation intensity at which the stimulated emission rate is half the spontaneous emission rate Γ . It is well-known that, if spontaneous emission is the dominant dephasing mechanism, the coherence decay rate is half that of the population decay rate [4], i.e., $\gamma_{13} = \gamma_{23} = \Gamma/2$. For the ^{87}Rb D1 transition the excited state spontaneous

emission rate $\Gamma = 2\pi \times 5.75$ MHz, and $\lambda = 794.98$ nm [5], yielding a value of 1.5 mW/cm² for I_{sat} from Eqn. 8. Our coupling intensity I varies between 0.15 and 5.6 mW/cm² (see Sec. 4 C below), which from Eqn. 8, corresponds to $|\chi_c|/2\pi$ ranging from about 1 to 8 MHz. The ground state decoherence rate $\gamma_{12}/2\pi$ is ≈ 3 kHz as reported in the literature [24] which is consistent with our own measurements in Sec. 6 below. Note that the probe detuning Δ_p is tens of kHz in our experiment, not tens of MHz as shown in Fig. S2 - see Sec. 6A for the explanation. Thus, our experiments are indeed conducted in the strong intensity limit defined in Eqn. 41.

To see how the condition in Eqn. 44 is satisfied in our experiments, we note that the Rb number density N is $2 - 4 \times 10^{11}/\text{cm}^3$ (see Fig. 7(a); our vapor temperature ranges from $55^0 - 65^0\text{C}$), and the dipole matrix element $|\mu_{13}|$ for the ^{87}Rb D1 transition is 2.54×10^{-29} Cm [5]. This yields $\frac{1}{2\pi} \sqrt{\frac{N|\mu_{13}|^2}{2\epsilon_0\hbar}} \omega_p \approx 2 - 4$ GHz which is comfortably larger than $|\chi_c|/2\pi$ (in the several MHz range as mentioned above). Further, note from Eqn. 43 that the group velocity varies inversely with the atomic number density N . This explains the need to heat the vapor cell in our experiments, as described in Sec. 5B below.

Evidently, from Fig. S2 and Eqn. 43, a necessary condition for producing slow light is the creation of a steep positive gradient in refractive index within a narrow spectral window where EIT is achieved. The narrower the spectral width of the EIT window (i.e., the tighter the pinch in the n_r -curve in Fig. S2(b)), the larger $dn_r/d\omega$, thus yielding slower v_g . Conversely, mechanisms that broaden the EIT window as described in Sec. 3B below, will serve to reduce the light slowing effects.

We end this section by addressing an issue that often confuses students. It is important to understand that the dramatic change in n_r near resonance in Fig. S2(b) does not much impact the *phase velocity* of light (defined as c/n_r) because n_r *never departs significantly from unity* for a dilute vapor - this is clearly visible in Fig. S2(b). One may visualize there being a “kink” or “pinch” near zero pump-probe detuning in the n_r -curve which is otherwise flat. No physical significance is ascribed to the phase velocity, so the fact that n_r dips below unity causing the phase velocity to exceed c is no cause for alarm. Recall that information and energy carried by a light pulse propagates at v_g , not the phase velocity [25].

3. Creation of three-level atomic system for EIT

As indicated above, the narrower the EIT window the slower the group velocity of light propagating through the medium. To combat broadening of the EIT line width and reduction in contrast, unwanted contributions from energy-levels that are extraneous to the three-level scheme in Fig. S1(a) must be avoided as far as possible.

Our experiments are performed on the D1 transition $5^2S_{1/2}, F_g = 2 \rightarrow 5^2P_{1/2}, F_e = 1$ in ^{87}Rb atomic gas. The 87 isotope is chosen over ^{85}Rb because, as depicted in Sec. 2 of the Supplementary Notes [14], the hyper-

fine levels in ^{87}Rb are farther spaced. The D1 transition is preferred to D2 for the same reason with regard to the excited state splittings. The Doppler broadening of Rb vapor at room temperature is about 500 MHz (see Sec. 3 B below), which is comparable to the excited state splitting for the ^{87}Rb D1 transition. This means that, even in the case of the ^{87}Rb D1 transition, the hyperfine excited levels partially overlap at room temperature, creating extraneous channels for atomic population to “leak” to, diminishing the steady-state fraction of atoms settling into the dark state (see Sec. S1 above). This loss of coherence is significantly more severe if either of the D2 transitions or the ^{85}Rb D1 transition is employed, for which the Doppler broadening exceeds the excited state splittings [14].

In our experiments Doppler broadening is highly suppressed by inserting a buffer gas into the sample (see Sec. 3 B below). However, even in this case, a pump or probe laser tuned near-resonance to a particular $F_g \rightarrow F_e$ transition will off-resonantly pump other close-lying F_e states. It is therefore advantageous for slow light experiments to use the ^{87}Rb D1 transition, for which the two F_e levels are farthest separated (compared to both D2 transitions, and the D1 transition in ^{85}Rb).

A. Zeeman EIT: Spin polarization via optical pumping

Three-level schemes with alkali atoms for EIT-based slow light experiments fall into two categories: Hyperfine EIT and Zeeman EIT, depicted in Figs. 3. These three-level schemes are referred to as “lambda-systems” because the two lower-levels are close-lying compared to their separation from the excited level, which means that the three levels form a Λ -shaped configuration.

As shown in Fig. 3(a), the hyperfine $5^2S_{1/2}$ ground state for the D1 transition is split by the interaction of the valence electron’s total angular momentum (orbital + spin) with the nuclear spin, creating $F_g = 1, 2$ ground energy states separated by 6.8 GHz. Hyperfine EIT with Rb requires an expensive electro-optic modulator to split off a weak sideband (probe; dashed line) from the main carrier (coupling beam; solid line), each beam tuned to an $F_g \rightarrow F_e$ transition - alternatively, one may employ two phase-locked lasers, each tuned to either transition.

Zeeman EIT is far less resource-intensive, requiring less expensive acousto-optical modulators and on a single passively-stable laser system. Hence we confine our attention to this method. In Zeeman EIT, the application of a small magnetic field B_z along the z -axis splits the degeneracy in each hyperfine level F creating $2F + 1$ magnetic substates, as depicted in Fig. 3(b). Zeeman EIT relies upon optical pumping of the magnetic Zeeman sub-levels with coupling and probe beams of mutually orthogonal circular-polarization, propagating along the z -axis, collinear with the Zeeman magnetic field B_z . Because B_z is created by a solenoid (see Sec 5C below) we refer to the z -direction as the axial, or longitudinal, direction.

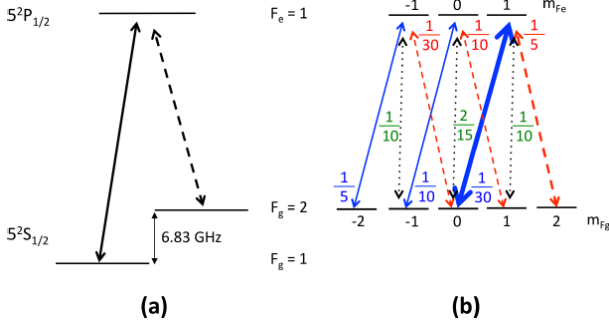


Fig. 3. Three-level lambda schemes for a) hyperfine EIT and b) Zeeman EIT. In (b) relative transition strengths are indicated for σ^+ (solid lines), σ^- (dashed lines), and π (dotted lines) transitions [26]. The ground states $m_{F_g} = 2, 0$ and the excited state $m_{F_e} = 1$ approximate the three levels $|1\rangle, |2\rangle, |3\rangle$, respectively, in Fig. S1(a).

In Fig. 3(b) we depict a strong σ^+ coupling field (solid arrows) and weak σ^- probe field (dashed arrows), tuned to near-resonance with the $5^2S_{1/2}, F_g = 2 \rightarrow 5^2P_{1/2}, F_e = 1$ transition. Assume the atoms are illuminated for times long compared to the excited state lifetime. The coupling field optically pumps most of the atoms into the $m_{F_g} = 1, 2$ spin sub-states: This happens due to the dipole selection rules for transitions induced by σ^+ light, which are $\Delta m = +1$ for absorption and $\Delta m = -1$ for stimulated emission, in addition to the $\Delta m = 0, \pm 1$ selection rule for spontaneous emission transitions. The presence of the weak σ^- probe means that the atomic population is mostly concentrated in the $m_{F_g} = 0, 2$ spin sub-states: Atoms falling into the $m_{F_g} = 1$ state are optically pumped (dashed arrows) toward the $m_{F_g} = 0, -1, -2$ states, where the atoms are again picked up by the strong σ^+ coupling beam (solid arrows) and brought back to the right hand side of the diagram. Optical pumping times of $\sim 0.5 - 1 \mu\text{s}$ are adequate for “spin-polarizing” in this manner alkali atoms such as Na, Rb, and Cs (with excited state lifetimes $\sim 16 \text{ ns}, 27 \text{ ns}$, and 31 ns , respectively [20]). Once the atoms are spin-polarized by optical pumping to approximate a three-level system, they evolve into the dark state (Sec. S1 above), thus enabling EIT and slow light.

Note that the ideal three-level lambda system (states $|1\rangle, |2\rangle$, and $|3\rangle$ in Fig. S1) is well-approximated in Fig. 3(b) by the ground states $m_{F_g} = 2, 0$ and the excited state $m_{F_e} = 1$, respectively. The thick solid arrow and rightmost dashed arrow in Fig. 3(b) correspond to ω_c and ω_p , respectively, in Fig. S1. Because the Zeeman shifts between the magnetic sub-levels of the $F_g = 2$ ground state are 0.7 KHz/mG [5], and B_z in our case is 50 mG (see Sec. 5C below), the Zeeman splittings for the $F_g = 2$ ground state range over $\sim 140 \text{ KHz}$. Note that the assumption at the beginning of Sec. S1, that the coupling beam only addresses levels $|2\rangle$ and $|3\rangle$ and the probe beam only addresses levels $|1\rangle$ and $|3\rangle$, is automatically satisfied in Zeeman EIT because the σ^+ pump photons

cannot be absorbed by the $|m_{F_g} = 2\rangle \rightarrow |m_{F_e} = 1\rangle$ transition and the σ^- probe photons cannot be absorbed by the $|m_{F_g} = 0\rangle \rightarrow |m_{F_e} = 1\rangle$ transition.

B. EIT linewidth broadening mechanisms

There are several deleterious factors that limit the fraction of atoms settling into the dark state, affecting the EIT linewidth and/or contrast. In this subsection we discuss these undesirable mechanisms and how to suppress them in most cases by using an inert buffer gas.

Collisions:

If spin-polarized Rb atoms collide they can exchange their valence electron. These spin-exchange collisions can redistribute the populations in the magnetic sub-states, rapidly destroying the spin polarization. Significant spin relaxation is also caused when spin-polarized atoms collide with the glass walls, as the atoms migrate across the vapor cell. A popular method to highly suppress both types of collisions is to insert an inert buffer gas [27]. The usual practice is to mix anywhere from a few Torr to several tens of Torr of a noble gas such as Neon, with several microTorr of alkali vapor. Rb-Rb collisions are negligible compared to Rb-Ne collisions. A Rb-Ne collision causes the Rb atom’s velocity to change but very little spin relaxation of the polarized Rb atom occurs.

Atomic transit time:

A significant form of spin relaxation is caused by the atoms simply exiting the pump laser beam. In a vapor cell with no buffer gas an average interaction time can be straightforwardly estimated by taking the ratio of the pump beam diameter and the 1D root-mean-square thermal atomic speed $\sqrt{k_B T/m}$, where k_B is the Boltzmann’s constant, T is the temperature in Kelvin, and m is the Rb atomic mass. Assuming a $1/e$ -diameter of 5 mm and an rms speed of $\sim 170 \text{ m/s}$ at room temperature ($T = 293 \mu\text{K}$, $m = 85 \times 1.67 \times 10^{-27} \text{ kg}$, $k_B = 1.38 \times 10^{-23} \text{ J/K}$), we calculate a transit time τ_{tr} of about $30 \mu\text{s}$, which yields an estimated transit time-broadened EIT linewidth $(2\pi\tau_{tr})^{-1}$ of just over 5 KHz. A rigorous derivation of the transit time broadened linewidth which includes optical pumping effects in a transiting three-level atom yields a value higher than our simple estimate by about a factor of two [28]. The inclusion of a buffer gas at several Torr of pressure induces a sufficient rate of Rb-Ne collisions that the frequent velocity-changing collisions effectively prevent the atoms from leaving the pump beam, thus highly suppressing transit time broadening of the EIT linewidth [29].

Doppler broadening:

The absorption profile of Rb vapor, illuminated by a frequency-scanning monochromatic beam, is Doppler-broadened owing to the thermal motion of the atoms [30]. In a simple 1D situation, an atom moving with thermal velocity v_{th} toward or away from a laser beam of frequency ν_0 sees a Doppler-shifted frequency $\nu_0(1 \pm v_{th}/c)$. This means that for a thermal distribution of velocities we may estimate the Doppler broadening Γ_D

of the absorption profile to be $\Gamma_D = 2\nu_0 v_{th}/c = k v_{th}/\pi$. Here we have used $c/\nu_0 = \lambda = 2\pi k$ where λ is the wavelength, and k is the magnitude of the incident field wave vector. If we use the most probable velocity $\sqrt{2\ln 2 k_B T/m}$ for v_{th} , we obtain $v_{th} \approx 200$ m/s at $T = 293$ μ K, yielding $\Gamma_D \approx 500$ MHz at $\lambda = 795$ nm.

The collinear pump-probe beam geometry is chosen to ensure that the atoms experience the same Raman detuning Δ' , i.e., different velocity classes of atoms resonantly interact with correspondingly Doppler-shifted illuminating frequencies, but the relative pump-probe detuning remains the same. However, it is experimentally impossible to perfectly co-align two distinct beams. A slight angle θ between the pump and probe beams leads to a *residual* Doppler broadening Γ_{RD} which we can straightforwardly estimate for the case when no buffer gas is present. To calculate the residual Doppler broadening Γ_{RD} , we introduce the coupling (i.e., pump) wave vector \vec{k}_c and the probe wave vector \vec{k}_p , both of equal magnitude $2\pi/\lambda$ but with a small angle θ between them. We find that $\Gamma_{RD} = |\vec{k}_c - \vec{k}_p| v_{th}/\pi \approx k v_{th} \theta/\pi = \Gamma_D \theta$. Thus, even for a slight relative angle $\theta \sim 0.1$ mrad, we find Γ_{RD} is significant: ~ 50 KHz.

Conveniently, the inclusion of a buffer gas at several Torr of pressure induces frequent velocity-changing collisions that act to tightly spatially confine each Rb atom. More precisely, the mean free path of the Rb atoms between collisions is comparable to the optical wavelength. One may say that in order to “sense” a Doppler shift in the frequency of an incident wave, an atom must maintain a certain velocity while being impinged by two consecutive wave-crests, but is prevented from doing so owing to frequency velocity-changing collisions with buffer gas atoms. Thus the Doppler-broadening of the absorption spectrum is highly suppressed.

Power broadening:

Evidently, from Eqn. 32 (along with Eqn. 8) and Eqn 43 (along with Eqn. 44), in the high coupling-intensity limit the group velocity v_g of the slowed light pulse depends linearly on coupling intensity I , as does the EIT linewidth, i.e., power-broadening occurs. On the other hand, lowering the coupling intensity too far (while still staying in the high coupling intensity limit) may reduce the steady-state fraction of atoms in the dark state to the point where slow light effects start to degrade and the slowed light pulse starts to speed up again. Thus we may expect a “sweet spot” in the coupling intensity where the conditions for slow light are optimized. This is borne out by experimental data in Sec. 6 D below.

Note that we neglect radiation trapping effects because they are expected to be significant at an atomic density at least an order of magnitude larger than the density $\sim 3 \times 10^{11}/\text{cm}^3$ used in our experiments [31].

4. Optical setup

In this section we describe the optical setup and how we create pump, probe, and reference beams of required

size, intensity, temporal width, and polarization purity.

A. Optical layout for slow light experiment

Our optical layout is depicted in Fig. 4. In our setup we use a commercial external cavity tunable diode laser (ECDL) to provide light at ~ 795 nm. A few percent of the output is split off for use in a saturated absorption spectroscopy (SAS) set-up to enable the precise tuning of the laser to the $F_g = 2 \rightarrow F_e = 1$ D1 transition (see Ref. [13], for example, for a discussion of SAS).

The main ECDL output is first passed through a Faraday rotation-based optical isolator (OI), then passed through an anamorphic prism pair to circularize the elliptical cross-section of the beam, before coupling into a single-mode polarization-maintaining fiber (we measured a residual polarization drift of less than 2%). The purpose of the Faraday rotator is to optically isolate the laser from back reflections arising, for example, from the optics that couple the light into the single-mode fiber.

B. Creating the pump and frequency-scannable probe

The output from the fiber (~ 7 mW) is collimated using an aspheric lens. The collimated light is divided by a polarizing beamsplitter (PBS 1) into two orthogonally linearly polarized beams - a strong coupling (or pump) beam (solid line) and a weak probe beam (dashed line).

A standard feature of pump-probe spectroscopy is that the probe is scanned in frequency around the fixed pump frequency, and the probe transmission spectrum is detected. The scanning is accomplished with an acousto-optic modulator (AOM), aligned in double-pass configuration to suppress spatial motion of the beam while frequency-scanning [32]. Because the AOM always introduces a frequency-offset and the scanning occurs around this offset frequency, we must insert an identically configured AOM in the path of the pump beam as well, so that both the pump and probe beams are offset in frequency by the same amount. In our experiments a waveform generator created an 80 MHz, 1 V signal which is amplified using a standard RF amplifier to drive each AOM with a single-pass efficiency of $\sim 70\%$. Planoconvex lenses of focal length 30 cm are placed on either side of each AOM, separated by approximately twice their focal length with the AOM crystal located halfway at the common focal spot. In our experiments, the -1 order is retroreflected by a quarter wave plate and mirror back through the AOM. Thus the -2 order is orthogonally polarized to the incident beam and counter-propagates along the incident beam path. The double-passed and incident beams are separated by a polarizing beamsplitter, PBS 2 for the pump and PBS 3 for the probe in Fig. 4.

C. Pump and probe beam size and pump intensity

The probe beam $1/e^2$ -radius is 1.13 mm. In order to approximate the assumption of an ideal plane coupling field (see Sec. 1 in Ref. [14]) the pump beam is expanded using a telescope comprising two plano-convex lenses so

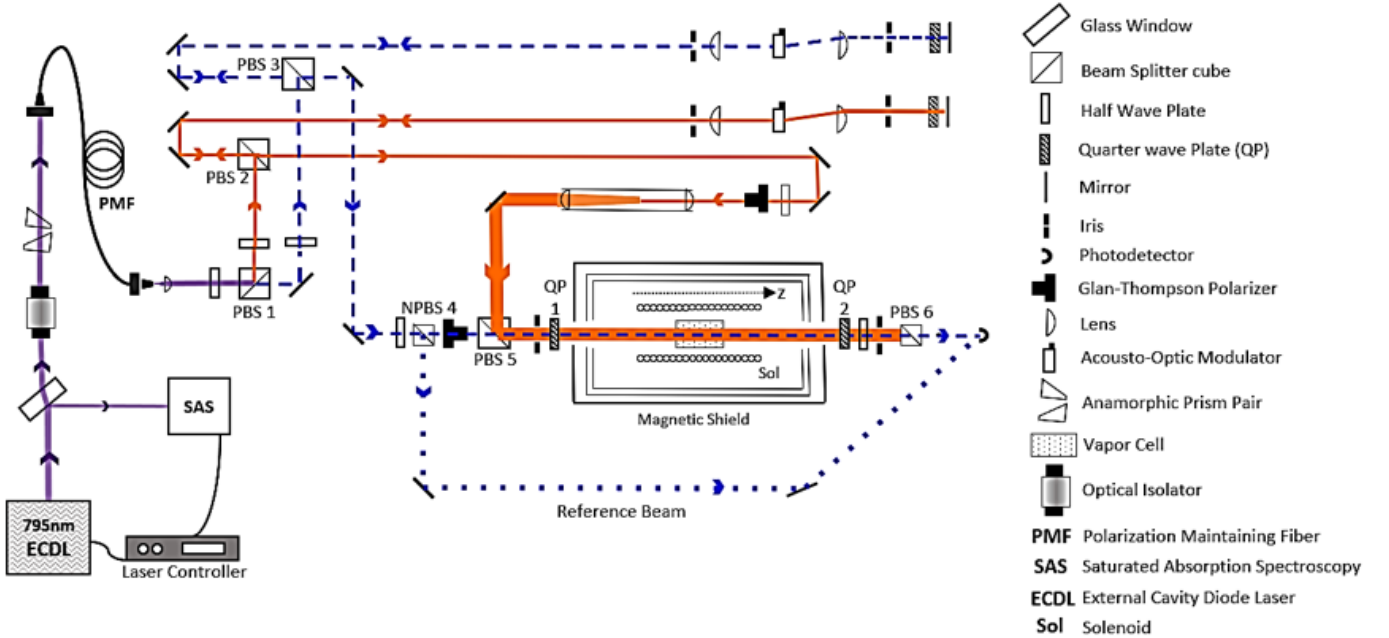


Fig. 4. Optical setup. The laser is split at a polarizing beamsplitter (PBS 1) into a strong pump, or coupling, beam (solid lines) and a weak probe beam (dashed lines). Before entering the vapor cell the probe beam is split at a non-polarizing beamsplitter (NPBS 4) to create a reference beam (dotted lines) for the slow light measurement. The z -axis is indicated.

that just before entering the vapor cell the pump beam has a $1/e^2$ -radius of 2.26 mm. The pump intensity was mostly varied between 1.25 and 5.6 mW/cm², though in a few cases was kept as low as 0.15 mW/cm². For comparison, we remind the reader that I_{sat} for the ⁸⁷Rb D1 transition is 1.5 mW/cm² (see Eqn. 8).

D. Probe and reference pulses and probe intensity

In our experiments, the probe beam is in the form of a short (temporal) Gaussian pulse. Slow light demonstrations consist of measurements of the delay of the probe pulse propagating through the sample relative to an identical reference pulse propagating a similar path-length outside the sample. This reference pulse, depicted by the dotted lines in Fig. 4, is split off from the probe pulse by inserting a non polarizing beamsplitter NPBS 4 into the probe path, as shown. The probe and reference pulses are created via amplitude modulation of the probe AOM by pulsing its rf-driver with a waveform generator.

The requirement to match the reference pulse path-length to the probe path is extremely forgiving in practice because a distance of 30 cm in air takes light only about a nanosecond to travel, which is negligible compared to the slowing produced in our experiment (several tens of microseconds as we see in Sec. 6B below). Both pulses are eventually made incident on the same photodetector, and the delay in their arrival times is measured on an oscilloscope by alternately blocking and unblocking each pulse. Because the pulse durations are on the order of microseconds (see Sec. 6 below) the detector is switched to a 10 k Ω output impedance to dampen signal reflections between the detector and oscilloscope.

The durations of the Gaussian probe and reference pulses must be long enough that the pulse frequency-

bandwidth (estimated as the inverse of the $1/e$ -pulse-duration) fits inside the EIT spectral window. According to Eqn. 32 the EIT linewidth broadens linearly with pump intensity, necessitating the use of probe pulses of progressively longer duration as the pump intensity decreases. Due to technical reasons, in order to use the same modulation amplitude as described above, we have to keep the probe pulse duration constant. Therefore, we end up selecting a suitably long probe pulse duration for which the frequency bandwidth fits inside the EIT line width for the entire range of pump intensities employed (see Sec. 6A below for details).

The probe intensity must be kept significantly less than the pump in order to satisfy the weak probe assumption. However, the probe pulse is too short to register on a typical power-meter. Therefore we illuminated a fast photodiode with continuous-wave light of known intensity, and calibrated the response in volts (as measured on an oscilloscope) per mW. Next, the probe pulse was shone upon the diode and the shape of the voltage response recorded. The probe beam (hence, also the reference pulse) is prepared to be a Gaussian temporal waveform - it is straightforward to measure time-delays between the centers of such pulses. In our case the pulses have a $1/e$ -width of 170 μ s, and the *peak of the probe Gaussian temporal waveform* is set at 0.3 mW/cm² (the average intensity of the Gaussian probe pulse is 0.12 mW/cm²). Thus, the weak probe assumption is well-satisfied in all our measurements where we used a pump intensity of 1.25 to 5.6 mW/cm². In a few cases, however, the pump intensity was as low as 0.15 mW/cm², comparable to the average probe intensity.

E. Polarization purity of pump and probe beams

An important experimental consideration in the weak probe regime is that when the pump and probe beams are recombined at polarizing beamsplitter PBS 5 just prior to entering the vapor cell (see Fig. 4), even a tiny polarization impurity in the pump causes leakage of the pump into the probe beam leading to a significant spurious enhancement of probe power: For the highest pump powers used in our experiment we find that a 0.1% polarization-impurity in the pump more than doubles the power in the probe polarization. Further, pump leakage may distort the shape of the probe pulse because the pump-profile is not entirely flat. It is, therefore, important to suppress as best as possible pump leakage into the probe owing to polarization impurity.

Polarization impurity is suppressed by the use of a Glan-Thompson polarizer (G-T; extinction ratio $10^5:1$) in the pump and probe beams. A half-wave plate is placed before each G-T to adjust the pump and probe intensities directed toward the vapor cell. Because of the large pump beam size, the half-wave plate and G-T for the pump beam are located before the beam expander. The polarizing beamsplitter at which the pump and probe beams are recombined has the property that 99.5% of *s*-polarization (light polarization normal to plane of incidence) is reflected whereas only 90% of *p*-polarized light (light polarization parallel to plane of incidence) is transmitted. In our setup, *s* is vertical polarization (perpendicular to the optics table surface) and *p* is horizontal (parallel to the table surface). For this reason the pump beam, which must be strong, is chosen to be *s*-polarized, and the probe is *p*-polarized.

Just before entering the vapor cell the combined pump and probe beams, which are still orthogonal-linearly-polarized, are passed through a quarter-wave plate (QP 1 in Fig. 4) and converted to orthogonal-circularly-polarized, as is required for the Zeeman EIT lambda-scheme. The beams are aligned into the vapor cell and irises are inserted to assist in day-to-day alignments.

A second quarter-wave plate (QP 2) placed after the vapor cell converts the σ^+ and σ^- polarizations back to linear so that the pump can be separated from the probe at a polarizing beamsplitter (PBS 6 in Fig. 4). A half-wave plate placed just after QP 2 is adjusted so that the probe cleanly transmits through PBS 6 and is focused onto a photodiode, while the pump is reflected away. The probe transmission spectrum is recorded via a fast photodiode connected to a digital oscilloscope (see Sec. 4D above). The impedance of the detector is kept low in order to reduce electrical reflections in the BNC cable between the detector and oscilloscope, at the cost of reduced overall voltage signal.

Despite careful attempts to suppress polarization impurity there is residual pump leakage into the probe due to, we suspect, a combination of using low-order wave plates (as opposed to zero-order wave plates) and a residual error in aligning QP1's optical axis to 45° with respect to the input beam polarizations. To minimize this

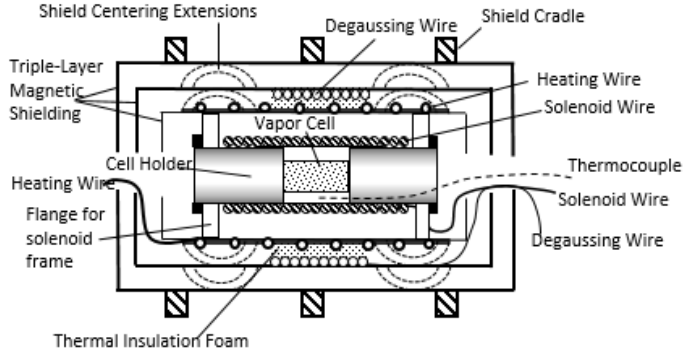


Fig. 5. Cross-sectional view of the components inside the zero gauss chamber used for applying a small axial magnetic field to enable Zeeman EIT, suppressing stray magnetic fields that broaden EIT linewidth, and heating the vapor cell to increase the atomic density participating in EIT. See text for further explanation of the components.

residual pump leakage we insert an iris after PBS 6 and close it down to roughly the size of the probe beam.

5. Magnetically shielded, warm vapor with applied magnetic field for Zeeman EIT

This section describes our magnetic shielding to suppress stray magnetic fields thereby creating a “zero gauss chamber” around the sample, the solenoid design which we use to apply a small B -field (~ 50 mG) to the alkali sample in a direction co-linear with the laser beam in order to enable Zeeman EIT, and the implementation of a heater system to raise the temperature of the alkali vapor in order to increase the atomic density participating in EIT. The zero gauss chamber and all the components inside it are shown in Figs. 5-7. In Sec. 3 of the Supplementary Notes [14] we describe in detail how to suppress below 0.2 mG any stray magnetic fields in the laser-atom interaction region.

A. Magnetic shielding:

As shown in Fig. 5 the chamber itself is formed by three layers of mu-metal sheets, each of thickness 0.025", in the form of open concentric cylinders. The outermost cylinder is 17.25" long, with a diameter of 8.25". The innermost cylinder's length is 15" and inside diameter is 6". Mu-metal alloy has high magnetic permeability and is specially engineered to divert incident magnetic field lines to ride along the material walls rather than penetrate through. A mu-metal end-cap on either end of the triple-shield forms a closed chamber which suppresses by a factor of 1500 any external magnetic fields leaking through. Two holes, about an inch in diameter, are drilled into the end-caps to allow the pump and probe laser beams through (and also, as shown, wiring leads for the solenoid, the heater wire, the thermocouple, and the degaussing current). The inner layers of the shield have rounded extensions attached on the outside as shown, which concentrically locate each shield at the radial cen-

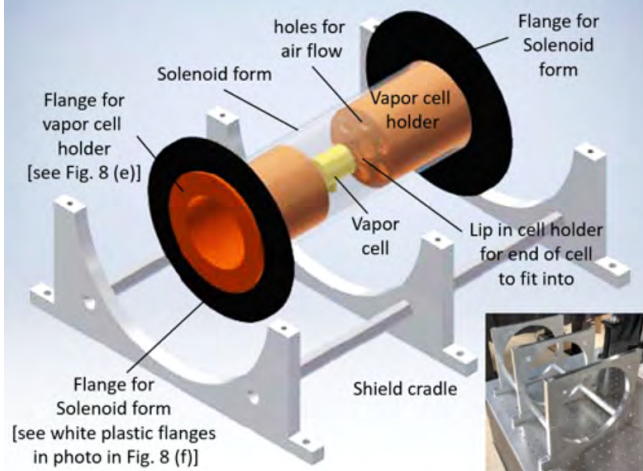


Fig. 6. A 3D view of the components inside the zero gauss chamber, with the shields and solenoid wiring removed to display the vapor cell and holders. The holders are drawn slightly back to reveal the lip in which the ends of the vapor cell securely fit. The diameter of the black flanges for the solenoid frame are machined to be a close slide-fit inside the innermost mu-metal cylindrical shield. The inset shows the complete aluminum cradle for housing the zero gauss chamber and locking it to the table.

ter of the larger shield it is placed in. The extensions did not protrude outward enough, causing inner layers to be shifted and rotated. Inserting a few strips of thermal tape to fill the ~ 3 mm space between each extension and the outer shield is the simplest fix for this problem.

An aluminum cradle houses and locks the zero-gauss chamber to the table. The cradle consists of three upright square plates, each with semi-circular cutouts for the chamber to rest in, as shown in Fig. 6. Semi-circular arches screw into the top of each piece to lock the chamber in place, as shown in the inset in Fig. 6.

B. Heated alkali vapor cell and cell-holder:

In our experiments, we employed two different types of cylindrical pyrex glass vapor cells, each one inch in diameter, filled with isotopically pure ^{87}Rb vapor and Ne buffer gas. The demonstration of slow light is carried out in a cell of length 1 inch (plus two $1/16$ -inch windows on either end) which is filled with 10 Torr of atomic Ne buffer gas. The temperature of the cell was varied between 55° and 65°C during the experiment. The other cell, of length 2 inches (plus $1/16$ -inch windows on either end) and 30 Torr Ne buffer gas, is used in an important auxiliary measurement to measure and suppress stray residual magnetic fields, besides also ensuring the efficacy of the degaussing procedure for the magnetic shields (see Sec. 3 of Supplementary Notes [14]). The purpose of the buffer gas is to mitigate undesirable EIT line-broadening effects described in Sec. 3B above.

As remarked earlier, toward the end of Sec. S1, we see from Eqn. 43 that in order to produce slower group

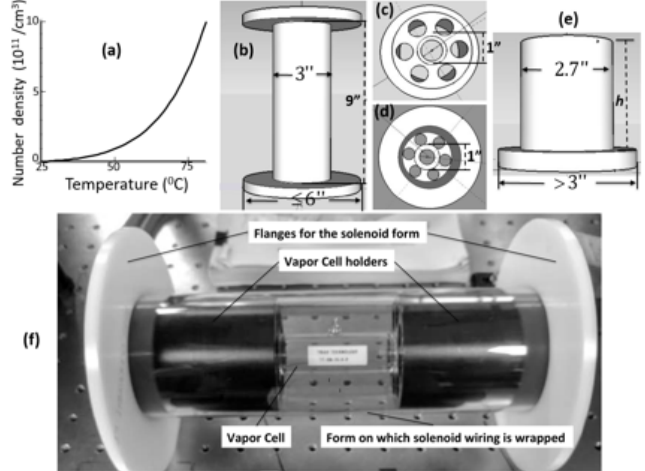


Fig. 7. a) Number density of atoms in vapor as a function of temperature. b) Side-view of the solenoid frame, before the wire is wound around the middle section between the flanges. c) Front view of one of the vapor cell holders (i.e., axial view of holder as seen looking outward from center of chamber where the vapor cell is located), showing holes cut into each holder for air-flow, and d) Back view of cell holder (i.e., axial view as seen from outside chamber). There are two holders, one for each side of the vapor cell. e) Side-view of a vapor cell holder. $h = 4$ inches for the 1 inch-long vapor cell, and 3.5 inches for the 2 inch-long vapor cell. f) Photograph of our solenoid frame (clear polycarbonate tube with white acetal flanges) before wrapping the wire, showing the vapor cell holders (black plastic), and glass vapor cell at the center.

velocity we need to raise the number density of atoms participating in EIT. We achieve this by heating the vapor cell and desorbing Rb atoms off the glass walls. A plot of the expected number density versus temperature is shown in Fig. 7(a) [5, 33].

Following the Novikova group at College of William and Mary [34] we directly wound an electrically insulated *non-magnetic* heating wire (see Fig. 5) around the outer surface of the innermost mu-metal shield, for heating the entire volume of space enclosed by the innermost shield. The wire is held firmly in place with thermal tape and a layer of thermally insulating foam. The vapor cell should be heated uniformly, so that “cold spots” not occur on the cell owing to thermal gradients [33–35].

The vapor cell fits securely inside a lip provided on each holder, as shown in Fig. 6. A rubber O-ring is placed in the lip on each end of the cell to prevent the cell from jostling around between the holders. The holders are a close slide-fit inside the solenoid frame, shown in Fig. 7(b), which is placed concentrically inside the innermost cylindrical mu-metal shield. Holes are cut into the cell holders, as shown in Figs. 7(c, d), to allow heated air to freely circulate, which significantly reduce the time needed for heating and increase the uniformity of the heating process. Flanges are provided on each holder,

on the side farther from the cell, which butt against the solenoid flanges (Figs. 6 and 7(e)), to prevent the holders from mechanically stressing the cell during assembly.

Further, it is important that the heating wires not cause any extraneous magnetic fields to circulate inside the zero-gauss chamber. We obtained 15 feet of non-magnetic heating cable, with two chromium wires in a twisted-pair configuration, yielding 9.5 turns around the innermost shield. These wires are coated in a flexible ceramic for high heat conduction. Current is sent through the first wire and is returned in the second wire. The magnetic fields created by the forward flowing current are almost negated by the magnetic field created by the backward flowing current, resulting in a net magnetic field which is nearly zero. Because heating wire is costly, we had to find a balance between price and number of turns needed for uniform heating of the mu metal chamber. The total resistance (forward and back combined) through the wire is 223 Ohms and the heater is rated for a maximum power of 90 W. While winding the heating wire around the inner shield, the heating wire was coated in a thermal paste to improve contact between the two metals. High temperature tape and foam were wrapped tightly around the heating wire to both insulate the heat from the outside and prevent the wire from shifting around and losing contact with the shield.

To accurately control the temperature of our vapor cell, we positioned a thermocouple (see Fig. 5) in the vicinity of the glass cell to automatically monitor the temperature and adjust accordingly the heating wire current supplied by a temperature controller. The controller measures the voltage on our thermocouple over a short time interval, and lets us set a desired temperature by selecting a reference voltage on the front control panel - then, using its built-in PID function the controller outputs a voltage corresponding to the difference between the measured and reference voltages. This output voltage is received by a solid-state relay which acts as a switch, turning on/off according to the voltage supplied to it, thus providing a cost-effective method to stabilize the laser temperature to within 0.1°C . Our thermocouple is type-T and its sensing tip is carefully located between the cell holders underneath the vapor cell no more than 3 cm away from the cell. We cannot measure the temperature of the vapor because it is sealed in the glass cell, but this placement of the thermocouple yields a reasonable estimate. In order to suppress the error in this estimate, we delayed starting experimental measurements by at least 30 minutes after the temperature stabilized on the thermocouple. During data-taking, we turn the heater off to be absolutely sure that any extraneous magnetic fields arising from the heater current are eliminated. The temperature drops by about $10-15^{\circ}\text{C}/\text{hour}$. Data collection is paused every few minutes and the heater turned on/off to maintain the temperature.

C. Solenoid

The Zeeman magnetic sub-levels are created by applying an axial magnetic field B_z of 50 mG, using the solenoid wiring depicted in Fig. 5. Ideally, the magnetic field needs to be completely uniform over the entire illuminated volume of the vapor cell. The uniformity of this magnetic field depends on the length to radius ratio of the solenoid. We referred to off-axis magnetic field calculations which plot magnetic fields strengths inside finite solenoids for varying length-to-radius ratios [36], and concluded that the length to radius ratio of the solenoid must be 6:1 in order to have a magnetic field tolerance of 1% at the furthest point from the center. The frame for the solenoid should be made from a sturdy plastic such as polycarbonate that does not soften at the temperatures used in our experiment. To center the solenoid inside the innermost mu-metal cylinder, the solenoid frame is fitted with white plastic flanges made of a less expensive plastic called acetal which are just under 6" in diameter. However, we find that acetal begins to soften at temperatures above 65°C , hence should not be used if an experiment requires higher vapor temperatures. Once softened, the flanges do not acquire their original shape upon cooling back down, compromising their good fit inside the innermost mu-metal cylinder.

Copper wire (gauge 21 or 22 is appropriate) is wound around the frame in two layers, with 220 turns/layer. The current I needed is calculated using $\mu_0 N_t I = B_z \sqrt{L^2 + 4r^2}$, where N_t is the number of turns, μ_0 is the magnetic permeability of vacuum, and B_z is the magnitude of the desired axial magnetic field [36]. We decided to use a radius r of 1.5" and length L of 9". Currents of less than 1 mA are needed to generate the small axial B -field needed for our experiments - we built an elementary circuit using a LM317HV current regulator capable of producing stable adjustable currents on the order of a μA with a potentiometer [37].

In Sec. 3 of the Supplementary Notes [14] we describe in detail how to suppress stray magnetic fields in the entire laser-atom interaction volume, which is a cylinder of diameter equal to that of the probe beam and length equal to that of the alkali vapor cell. We use a dedicated auxiliary optical pumping technique [6] to reduce the total stray residual magnetic field well below 0.5 mG (less than 1% of the Zeeman field B_z).

6. Results and Discussion

In this section we show our slow light results. The first step is to observe the EIT transparency window. The observed EIT linewidth helps us to determine a suitable pulse duration of the probe and reference pulses. As mentioned earlier (Sec. 4D), it is important to ensure that the width of the EIT spectral window exceeds the probe pulse bandwidth. Further, observing the EIT profile allows us to precisely tune our pump laser frequency to the center of the window where peak transparency occurs. Next, we measure the delay of the probe pulse that

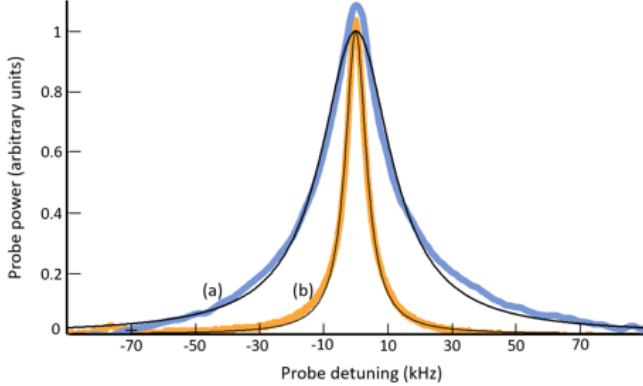


Fig. 8. (a) The measured EIT transparency line shape (thick line) for a pump intensity of 5.5 mW/cm^2 . The FWHM line width, extracted by a Lorentzian fit (thin black line), is 26 KHz. (b) For a pump intensity of 1.3 mW/cm^2 we determine the EIT line width to be 7.3 KHz. The graphs are scaled vertically so that the fits are normalized.

passes through the sample relative to a reference pulse that does not. Finally, we examine the dependence of the probe group velocity v_g on the coupling intensity I .

A. EIT linewidth measurement and probe pulse width

The EIT spectrum is located by scanning the probe frequency over a range larger than the Zeeman splittings of the $F_g = 2$ ground state in Fig. 3(b). The probe AOM frequency is offset to locate the EIT spectrum at the center of the scan. At this point, the ECDL current is also very slightly adjusted to finely vary the ECDL frequency in order to optimize the EIT spectrum.

Typical EIT linewidths measured for high and low pump intensities, as a function of the probe detuning Δ_p , are shown in Fig. 8. The graphs are normalized to allow for a comparison of the EIT linewidths at the two different pump intensities. In reality, the maximum contrast we obtain is only about 25%, much lower than theoretically predicted by Eqn. 27 and displayed in Fig. S2(b). We see that the EIT linewidth, too, is far narrower than theoretically predicted, for reasons already discussed in Sec. S1. We may directly compare the theoretically predicted EIT linewidth in Fig. S2(b) with the experimental linewidth in Fig. 8(b) because a pump intensity of 1.3 mW/cm^2 corresponds to $|\chi_c|/2\pi \approx 4 \text{ MHz}$ (from Eqn. 8): We note that the observed linewidth of 7.3 KHz is nearly three orders of magnitude narrower than the prediction of $\sim 6 \text{ MHz}$ which we read off directly from Fig. S2(b). The reason for the lower EIT contrast than theoretically predicted, and narrower EIT linewidth, was indicated already by us in Sec. S1: Our theory was performed for a single atom, not an optically thick atomic ensemble as is used in the experiment. In dense vapor the low contrast observed means that only the spectral components which lie at the center of the EIT transparency window can propagate through, causing a significant reduction in the observed linewidth [19].

In Ref. [19] the authors estimate how much the EIT window narrows by. They show that the power-broadened component of the predicted linewidth (i.e., the second term in Eqn. 32) is expected to reduce by a factor $1/\sqrt{\eta kL}$ where $\eta = 3N\lambda^3/4\pi^2$, $k = 2\pi/\lambda$, and L = length of the vapor cell. Using $N = 3.8 \times 10^{11}/\text{cm}^3$ (the number density at 65^0C for the data in Fig. 8) and $L = 2.5 \text{ cm}$, we find that $\sqrt{\eta kL} \approx 54$. Thus we may arrive at a revised predicted EIT linewidth by simply dividing the 6 MHz in Fig. S2(b) by 54 to obtain $\approx 110 \text{ KHz}$ which is much closer to the observed value than before, but still 15 times larger (using Eqn. 32, a less precise approximation than Eqn. 27, yields $\sim 200 \text{ KHz}$). It is remarkable we can get this close using a simple closed three-level model as described in this work. To better model the experiment, the theory must include the full hyperfine structure of ^{87}Rb [19].

While the simple three-level expressions in Eqns. 27 - 33 do not quantitatively reproduce the observed values, Eqn. 32 can be used along with the relation $|\chi_c|^2 \propto I$ (Eqn 8) to justify the scaling of the observed linewidth with pump intensity: Starting with the observed linewidth of 26 KHz in Fig. 8(a) and recalling from Sec. S1 that $\gamma_{12}/2\pi \approx 3 \text{ KHz}$, the power-broadened term in Eqn. 32 (i.e., the second term) must then be $\approx 20 \text{ KHz}$. This intensity-dependent term is scaled down by a factor ~ 4 in going from the high to the low intensity in Fig. 8. This means the expected linewidth in Fig. 8(b) is $2(3) + (20/4) \approx 11 \text{ KHz}$, not far from the observed linewidth of 7.3 KHz.

We chose a $1/e$ -width of $170 \mu\text{s}$ for our Gaussian probe and reference pulses (see Sec. 4D). The corresponding bandwidth of $\leq 1 \text{ KHz}$ is short enough to fit inside the EIT window which, from Eqn. 32, is at least $2\gamma_{12}/2\pi = 6 \text{ KHz}$ even for the smallest pump intensities.

Finally, note in Fig. 8 that the EIT data are spectrally narrower at the transparency center than the Lorentzian fits. This is ascribed to Ramsey-narrowing induced by atoms that diffuse out of the laser beam and return without decohering [24].

B. Measuring delay between probe and reference pulses

The probe frequency scan is now turned off, the probe AOM offset voltage is tuned to the EIT peak, and the amplitude modulation is turned on to create short pulses, as described in Sec. 4D. Once both slow and reference pulses were detected on our oscilloscope, the wave-form for each was fit to a gaussian curve, and the relative delay time δ extracted - this is just the time taken by the slowed pulse to propagate a certain distance L through the vapor minus the time taken by the reference pulse to travel the same distance through air. We calculated the group velocity v_g using

$$\delta = \frac{L}{v_g} - \frac{L}{c} \Rightarrow v_g = \frac{cL}{c\delta + L} \xrightarrow{c\delta \gg L} \frac{L}{\delta} \quad (9)$$

where $L = 1$ inch from Sec. 5B above. The inequality in the equation is satisfied for delays on the order of

several nanoseconds and beyond - in our case δ is in the microsecond regime. Note that the reference pulse travels an additional path length (see Fig. 4) compared to the probe pulse, but the extra time incurred is only ~ 1 ns.

Typical measurements of slow light are presented in Fig. 9, where the data (fuzzy lines) are shown along with Gaussian fits (smooth lines). In Fig. 9(a) the ref-

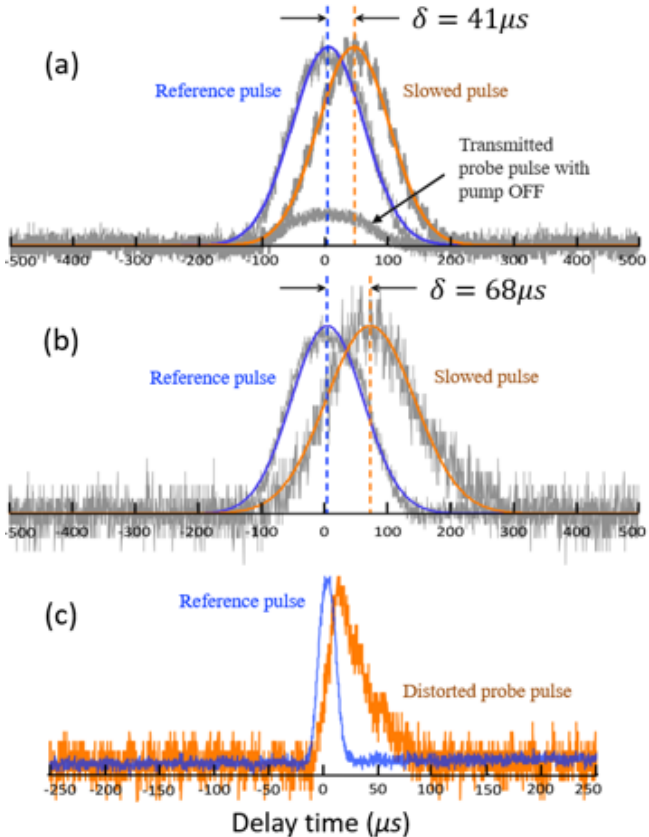


Fig. 9. Measurement of time-delay δ between a reference pulse traveling through air and the probe pulse traveling through the EIT medium. a) $\delta = 41 \mu\text{s}$ yields $v_g = 621 \text{ m/s}$. Pump intensity $I = 3 \text{ mW/cm}^2$. The squat data-curve is the transmitted probe pulse when the pump is blocked, in which case EIT ceases so that large absorption and no slowing occurs. b) $\delta = 68 \mu\text{s}$ yields $v_g = 361 \text{ m/s}$, our slowest observed velocity. Pump intensity $I = 1.2 \text{ mW/cm}^2$. c) Significant distortion in the transmitted probe pulse occurs if we select a pulse duration so narrow that the probe bandwidth does not fit inside the EIT transparency window. All measurements here were taken at 65°C .

erence pulse arrives at the detector $41 \mu\text{s}$ before the probe pulse, which corresponds to a slowed probe group velocity of 621 m/s . In Fig. 9(b) we show the slowest group velocity of 361 m/s , corresponding to a delay of $68 \mu\text{s}$, that we achieved with our setup. In each case, the peaks of the fits for reference and probe are scaled to the same value for easier comparison. The intensities of the reference and probe pulses are similar when they are split at the non-polarizing beamsplitter NPBS4 in Fig. 4, but the probe pulse suffers some absorption as it trans-

mits through the vapor - recall that our EIT contrast never exceeds 25% - which explains the larger noise levels on the slowed pulses. The slowest group velocity was achieved by lowering the pump intensity which further reduces the overall signal-to-noise ratio.

C. Role of EIT transparency window

Fig. 9(a) highlights the importance of the EIT process. The squat data-waveform visible in the plot is the transmitted probe pulse in the absence of the pump beam, causing the EIT window to cease to exist. Large absorption and no slowing is observed once the pump is blocked. The transmitted power of the slow pulse for the unblocked pump is $\sim 20 - 25\%$ of the incident probe power, while for the blocked pump is less than 5%.

To further highlight the important role played by EIT we show in Fig. 9(c) what happens if we select a pulse duration for which the probe bandwidth does not fit inside the EIT transparency window. The input Gaussian pulse in this case, namely $\sim 20 \mu\text{s}$ (which yields a $1/e$ -pulse bandwidth of $\sim 10 \text{ KHz}$), is nearly an order of magnitude shorter than the $170 \mu\text{s}$ pulse employed in Fig. 9(a) and (b). Thus, in the case of Fig. 9(c) the pulse bandwidth is comparable to the EIT window which ranges from a few KHz to $\leq 30 \text{ KHz}$ for our experiments. Therefore, certain frequency components of this pulse do not fit within the EIT window and are not slowed, instead getting significantly absorbed. This leads to a dramatic temporal stretching and distortion of the pulse, as shown in Fig. 9(c) (we scaled the vertical size of the reference pulse to about that of the transmitted probe).

In fact, some probe pulse broadening is even visible in the case of the slowest group velocity measured in Fig. 9(b). In this case, higher frequency components of the Gaussian probe pulse ($1/e$ -frequency bandwidth $\sim 1 \text{ KHz}$) extrude past the 7.3 KHz Lorentzian EIT transparency window, and are strongly absorbed. This causes an effective narrowing of the probe bandwidth, which leads to a broadening of the pulse duration.

D. Slow group velocity vs. pump intensity

In Fig. 10 we plot the experimentally observed slow light group velocity for several pump intensities at three different vapor temperatures. The observed temperature-dependence of v_g is in accordance with what we expect from Eqn. 43 and Fig. 7(a): The atom number density N increases with T , causing v_g to decrease.

At a fixed temperature we surmise from Fig. 10 that two competing slow light effects occur when we vary the pump intensity. The linear increase of v_g with increasing pump intensity I is expected from Eqn. 43 (in conjunction with Eqns. 8 and 44). Recall that this originates from the power-broadening of the EIT transparency window as described by Eqn. 32, and the need to “pinch the wrinkle” in the real refractive index n_r in Fig. S2(b) as described in Sec. S1. However, it is obvious that one cannot keep reducing the pump intensity to achieve lower and lower group velocities as there is no slow light in the

absence of a pump. At really low pump intensities the population of atoms being pumped to the dark state declines to the point that the group velocity starts creeping back up.

Thus there occurs a “sweet spot” in the coupling intensity at which the conditions for slow light are optimized. The lowest speed we achieved is 361 m/s at 65°C. A modest rise in temperature, by 10 to 20°C, would significantly further reduce v_g , possibly less than 100 m/s. The reason we did not proceed to higher temperatures is that the white plastic acetal flanges on our solenoid frame began to soften, as mentioned earlier in Sec. 5C. This choice of material is easily avoided in future designs.

7. Conclusion

We have presented detailed theoretical and experimental undergraduate-friendly instructions on how to produce light pulses propagating through warm alkali vapor with speeds as low as 361 m/s. We elucidated the role played by electromagnetically induced transparency (EIT) in producing slow light. Prices for key components and vendor information are included in Table 1.

8. Acknowledgements

We gratefully acknowledge financial support from the Army Research Office. We deeply appreciate invaluable discussions with Dr. Irina Novikova and Dr. David Phillips. We thank [names removed for reviewing purposes] for help during the initial setup. We are indebted to the Dean of the College of Arts and Science for providing generous seed funding to our advanced optics and lasers teaching laboratory for undergraduate seniors and first-year Masters’ students.

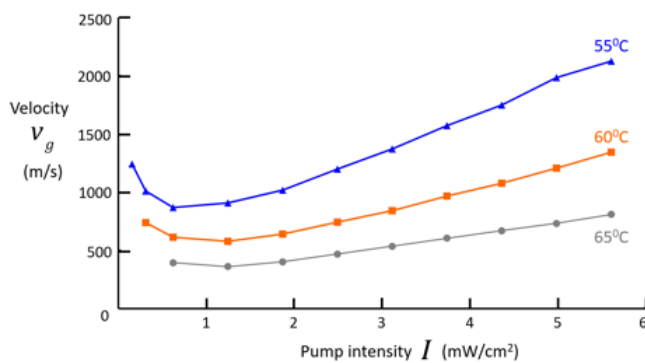


Fig. 10. Slow light at different pump intensities and temperatures (lines drawn to guide the eye). As temperature increases, causing an increase in atomic number density N , the velocity v_g is observed to decrease which is in accordance with the prediction by Eqn. 43. At fixed temperature, v_g is observed to increase with I for high pump intensities, in accordance with Eqn. 43. For really low intensities v_g creeps back up, yielding a “sweet spot” in intensity where slow light effects are optimized.

References

1. L. V. Hau, S. E. Harris, Z. Dutton, and C. H. Behroozi, “Light speed reduction to 17 metres per second in an ultracold atomic gas”, *Nature* **397**, 59459 (1999)
2. M. M. Kash, et al, “Ultraslow group velocity and enhanced nonlinear optical effects in a coherently driven hot atomic gas”, *Phys. Rev. Lett* **82**, 5229 (1999)
3. S. Harris, J. Field, and A. Imamoglu, “Nonlinear optical processes using electromagnetically induced transparency”, *Phys. Rev. Lett.* **64**, 1107 (1990)
4. S. Harris, “Electromagnetically induced transparency”, *Physics Today* **50**, 36 (1997)
5. I. Novikova, R. L. Walsworth, and Y. Xiao, “Electromagnetically induced transparency-based slow and stored light in warm atoms”, *Laser Photonics Rev.* **6**, 333-353 (2012)
6. L. Ma, O. Slattery, and X. Tang, “Optical quantum memory based on electromagnetically induced transparency”, *J. Opt.* **19**, 043001, 1-24 (2017)
7. M. Afzelius, N. Gisin, and H. D. Riedmatten, “Quantum memory for photons”, *Phys. Today* **68**, 6 (2015)
8. C. S. Adams, J. D. Pritchard, and J. P. Schaffer, “Rydberg atom quantum technologies”, *J. Phys. B* **53**, 012002 (1-13) (2020)
9. N. Belcher, E. E. Mikhailov, and I. Novikova, “Atomic clocks and coherent population trapping: Experiments for undergraduate laboratories”, *Am. J. Phys.* **77**, 988 - 998 (2009)
10. See, for example, A. Zheng, A. Green, M. Crescimanno, and S. O’Leary, “Electromagnetically-induced-transparency intensity-correlation power broadening in a buffer gas”, *Phys. Rev. A* **93**, 043825 (2016)
11. K. B. MacAdam, A. Steinbach, and C. Wieman, “A narrow-band tunable diode laser system with grating feedback, and a saturated absorption spectrometer for Cs and Rb”, *Am. J. Phys.* **60**, 1098 - 1111 (1992)
12. A. S. Arnold, J. S. Wilson, and M. G. Boshier, “A simple extended-cavity diode laser”, *Rev. Sci. Instrum.* **69**, 1236 - 1239 (1998)
13. A. Hachtel, J. Kleykamp, D. Kane, M. Marshall, B. Worth, J. Barkeloo, J. Kangara, J. Camenisch, M. Gillette, and S. Bali, “An undergraduate measurement of radiative broadening in atomic vapor”, *Am. J. Phys.* **80** (8), 740 - 743 (2012); *ibid.* **81**(6), 471 (2013)
14. See Supplementary Notes that accompany this article.
15. A. J. Olson and S. K. Mayer, “Electromagnetically induced transparency in rubidium”, *Am. J. Phys.* **77** (2), 116 - 121 (2009)
16. K. T. McDonald, “Slow light”, *Am. J. Phys.* **68** (3), 293 - 294 (2000)
17. T. Pang, “Electromagnetically induced transparency”, *Am. J. Phys.* **69** (5), 604 - 606 (2001)
18. P. W. Milonni and J. H. Eberly, “Laser Physics”, Wiley (2010), Sec. 9.10, pp 441 - 446
19. M. Lukin, M. Fleischhauer, A. Zibrov, H. Robinson, V. Velichansky, L. Hollberg, and M. Scully, “Spectroscopy in dense coherent media: Line narrowing and interference effects”, *Phys. Rev. Lett.* **79**, 2959 - 2962 (1997)
20. H. J. Metcalf and P. van der Straten, “Laser Cooling and Trapping”, Springer-Verlag New York, Inc (1999)
21. Eqn. 4.11.8 in Ref. [1] addresses the case of a sample with

Table 1. Key components used for the slow light experiment. Expensive items such as the external cavity tunable diode laser system (ECDL), and the mu-metal magnetic shield with degaussing capability, can be built in-house to cut costs [39–42].

Item	Model	Cost
ECDL, current/temperature control	Vitawave (Russia) ECDL7940R	\$ 8000 [39–41]
Anamorphic prism pair	Thorlabs PS871-B	\$ 164
Faraday Rotator	Conoptics 712B	\$ 1985 [43]
PM single mode fiber	Thorlabs P3-780PM-FC-2	\$ 197
Single mode fiber port (2)	Thorlabs PAF2A-11B	\$ 587 ea
Cage assembly	Thorlabs CP33 (plate); SR4 (rods)	\$ 211
AOMs (2)	Gooch and Housego 3080-122	\$ 660 ea
Waveform generator	Rigol DG4102	\$ 899
RF amplifier	Digikey	\$ 330
Glan-Thompson polarizer (2)	Thorlabs GTH10M-B	\$ 652 ea
Polarizing beamsplitters (3)	Newlight Photonics Inc. GPC 0210	\$ 549 ea
Nonpolarizing beamsplitter	Thorlabs PBS 252	\$ 253 ea
Half-wave plates (8)	Thorlabs BS 013	\$ 225
Quarter-wave plates (4)	Singapore Optics WP-05UM-LH-795	\$ 95 ea
Photodiode	Singapore Optics WP-05UM-LQ-795	\$ 95 ea
Mu-metal shield with degaussing wire	New Focus Inc. 1621	\$ 594
Heater wire (15 ft)	Magnetic Shield Corporation ZG-206	\$ 2130 [42]
Temperature controller	ARi Industries 2HN063B-13	\$ 6.67/ft
Thermocouple	Omega CN743	\$ 115
Vapor cells with Ne buffer gas	Digikey 317-1305-ND	\$ 3.18
	Precision Glassblowing TG-ABRB-I87	\$ 650 ea.

populations spread uniformly across all the ground Zeeman sub-levels. In subsequent paragraphs the authors in Ref. [1] modify Eqn. 4.11.8 to deal with the situation which applies to our experiments, i.e., where the atoms are optically pumped by circularly polarized light into the $m_{F_g} = +F_g$ (or $-F_g$) state.

22. See Sec. 9.4 in Ref. [1] for a nice description of how to include relaxation processes in the density matrix.
23. <https://steck.us/alkalidata/>, “Rubidium 85 D line data” and “Rubidium 87 D line data”, by Daniel Steck, University of Oregon
24. Y. Xiao, I. Novikova, D. F. Phillips, and R. Walsworth, “Diffusion-induced Ramsey narrowing”, *Phys. Rev. Lett.* **96**, 043601 (2006)
25. D. J. Griffiths, “*Introduction to Electrodynamics*”, 4th edition, Pearson, Inc (2013), Sec. 9.4.3, pg. 418
26. M. Auzinsh, D. Budker, and S. M. Rochester, “Optically Polarized Atoms”, Oxford Univ. Press (2010), pg. 141
27. Another popular method is to coat the inside of the glass cell walls with paraffin, which preserves the spin-polarization of the alkali atom in a collision with the wall. None of our cells in this work are coated.
28. J. E. Thomas and W. W. Quivers, Jr., “Transit-time effects in optically pumped coupled three-level systems”, *Phys. Rev. A* **22** (5), 2115 - 2121 (1980)
29. Instead of flying across, the atoms now slowly diffuse through the laser beam, thus highly suppressing transit time broadening effects. An expression for this residual diffusion-induced decoherence rate is provided in E. Arimondo, “Relaxation processes in coherent population trapping”, *Phys. Rev. A* **54** (3), 2216 - 2223 (1996)
30. See, for example, Ref. [1], Sec. 3.9, pgs. 105 - 108

31. A. B. Matsko, I. Novikova, M. O. Scully, and G. R. Welch, “Radiation trapping in coherent media”, *Phys. Rev. Lett.* **87** (13), 133601 (2001)
32. See Fig. 5 and accompanying text in J. Kleykamp, A. Hachtel, D. Kane, M. Marshall, N. Souther, P. Harnish, and S. Bali, “Measurement of sub-natural line width AC Stark shifts in cold atoms: An experiment for an advanced undergraduate laboratory”, *Am. J. Phys.* **79**(12), 1211 - 1217 (2011)
33. G. T. Purves, “Absorption and dispersion in atomic vapors: Application to interferometry”, PhD thesis, University of Durham (2006), pg. 25
34. N. B. Phillips, “Slow and stored light under conditions of electromagnetically induced transparency and four-wave mixing in an atomic vapor”, PhD thesis, College of William and Mary (2011)
35. M. J. Klein, “Slow and stored light in atomic vapor cells”, PhD thesis, Harvard University (2009)
36. E. E. Callaghan and S. H. Maslen, “The magnetic field of a finite solenoid”, NASA Technical Note D-465, E-900, 1 - 26 (1960)
37. K. DeRose, “Observations of slow light, stored light, and Dicke narrowing in warm alkali vapor”, M.S. thesis, Miami University, Oxford (2019)
38. M. Shuker, “Decay processes in EIT medium”, PhD thesis, Technion - Israel Institute of Technology (2008)
39. K. B. MacAdam, A. Steinbach, and C. Wieman, “A narrow-band tunable diode laser system with grating feedback and a saturated absorption spectrometer for Cs and Rb”, *Am. J. Phys.* **60** (12), 1098 - 1111 (1992)
40. P. Feng and T. Walker, “Inexpensive diode laser microwave modulation for atom trapping”, *Am. J. Phys.*

63, 905 - 908 (1995)

41. A. S. Arnold, J. S. Wilson, and M. G. Boshier, “A simple extended-cavity diode laser”, *Rev. Sci. Instrum.* **69** (3), 1236 - 1239 (1998)
42. S. Dickerson, J. Hogan, D. Johnson, T. Kovachy, A. Sugarbaker, S. Chiow, and M. Kasevich, “A high-performance magnetic shield with large length-to-diameter ratio”, *Rev. Sci. Instr.* **83**, 065108 (1-9) (2012)
43. This is the model we had available in the lab. It has a tuning range of 644 - 780 nm. However, the isolator still functions at 795 nm at the cost of a slight reduction in transmission. We measured an isolation level of -38 dB and a forward transmission of 86% (down from the advertised 92%). Models specified by Conoptics for the 700 - 900 nm range are 712GG and 713A.

SUPPLEMENTARY NOTES

Producing slow light in warm alkali vapor using electromagnetically induced transparency

Compiled March 18, 2022

In order to complement the undergraduate-friendly detailed experimental description in the main article, here we provide a detailed theoretical description of the basic physics behind slow light using electromagnetically induced transparency (EIT). In the sections below we follow closely the excellent treatment in Ref. [1], but include non-zero pump laser detuning, and a section on dark and bright states. We endeavor to keep the discussion amenable to advanced juniors and seniors. We include a background section on the atomic hyperfine structure of ^{87}Rb , and a final section on details of an auxiliary measurement to ensure that residual stray magnetic fields are suppressed below 0.2 milliGauss. © 2022 Optical Society of America

S1. Theoretical Background

The theoretical discussion of EIT and slow light centers around calculating the complex refractive index $n = n_r + in_i$ of the medium. The imaginary part n_i yields the absorption spectrum where EIT in atomic media is revealed as a narrow transparency window near resonance. The real part n_r yields the group velocity of light propagating through the medium. Slow light is revealed as a consequence of the steep frequency-variation of n_r within the EIT transparency window.

We begin by defining a three-level system, the simplest atomic energy-level configuration in which to elucidate the basic concepts of EIT and slow light. Next, we write down the Hamiltonian and the Schrodinger equation for this system, and derive the widely used optical Bloch equations. These equations are used to calculate the complex refractive index n of the gaseous sample, and reveal the required conditions for EIT and slow light.

A. Three-level system for EIT and slow light

Following the notation in Ref. [1] we depict a fictitious three-level atomic model in Fig. S1(a), in which transitions are allowed between states 1 and 3 and between states 2 and 3 but not between states 1 and 2. The standard EIT

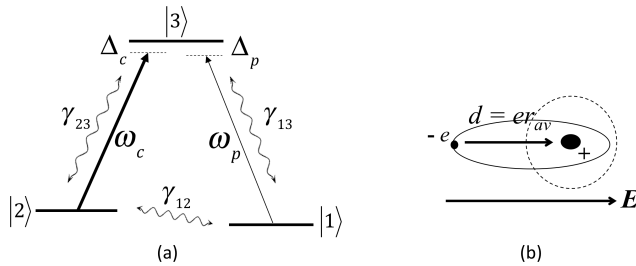


Fig. S1. a) Three-level atomic model. A strong coupling (or pump) beam of frequency ω_c and a weak probe beam of frequency ω_p , are both tuned to near-resonance with $|3\rangle$ from levels $|2\rangle$ and $|1\rangle$ respectively, with detunings Δ_c and Δ_p . Decoherence rates between levels 3 and 1, 3 and 2, 2 and 1, are denoted by γ_{13} , γ_{23} , γ_{12} , respectively (see Eqns. 19 and preceding text). b) Depiction of an atom showing a lone valence electron orbiting the nucleus (big dot). In the absence of an external field, the mean dipole moment, averaged over an electron revolution (circular orbit), is zero. When illuminated by an electric field \vec{E} , the electron cloud shifts in the opposite direction (elliptical orbit) creating an induced dipole moment \vec{d} of magnitude er_{av} , where $r_{av} (\propto E)$ represents the average displacement between the positive and negative regions of the atom. The polarizability α_p is defined by $\vec{d} = \alpha_p \vec{E}$.

experiment consists of a strong coupling (or pump) beam of frequency ω_c and a weak probe beam of frequency ω_p , both tuned to near-resonance with $|3\rangle$ from levels $|2\rangle$ and $|1\rangle$ respectively, with detunings Δ_c and Δ_p . We assume that the pump beam only addresses the coupling transition $|2\rangle \rightarrow |3\rangle$ and the probe beam only addresses the $|1\rangle \rightarrow |3\rangle$ transition. The probe frequency is scanned around the (fixed) pump frequency, and the probe transmission spectrum is measured.

B. Hamiltonian for light-atom interaction

If we denote the wavefunction for the atom interacting with an incident light field as $\Psi(\vec{r}, t)$, the time evolution of Ψ is described by the Schrödinger equation

$$i\hbar \frac{\partial \Psi(\vec{r}, t)}{\partial t} = \hat{H}\Psi(\vec{r}, t) = (\hat{H}_0 + \hat{V})\Psi(\vec{r}, t). \quad (10)$$

Here, \hat{H} is the Hamiltonian for the system, i.e., the energy operator (potential plus kinetic) of the system, acting upon the wavefunction Ψ . Since we are focusing on just the atom and its interaction with the incident field, we may ignore the contribution to the Hamiltonian from the incident field alone (also known as the free field). In that case it is convenient to express the Hamiltonian operator \hat{H} as a sum of two terms, where \hat{H}_0 is the bare Hamiltonian which describes the atom in the absence of any external field, and \hat{V} is the interaction Hamiltonian which describes the interaction between the atom and the external field.

Typically the outermost electrons of the atom are the least tightly bound and respond most readily to the incident field. Indeed, this is an important reason why alkali atoms are favorites with physicists - relatively low optical energies are needed to resonantly excite the lone valence electron. Further, the interaction of the single electron with the incident field is simple to model. The incident electromagnetic field's electric and magnetic vectors, $\vec{E}(\vec{r}, t)$ and $\vec{B}(\vec{r}, t)$ respectively, interact with the valence electron (negative charge e) through the Lorentz force. The electron speed is typically non-relativistic, so the effect of the \vec{B} -field may be ignored [2]. The $e\vec{E}$ -term in the Lorentz force induces an electric dipole \vec{d} in the atom (see Fig. S1(b)).

Thus, \hat{V} is given by the potential energy stored in this induced dipole, $\hat{V} = -\vec{d} \cdot \hat{\vec{E}}(\vec{r}, t)$ where \vec{r} is simply the location of the atomic center of mass. We ignore the variation of \vec{E} over the spatial extent of the atom (typically 0.1 - 1 nm) because the optical wavelength (typically hundreds of nm) is much larger.

For the simple three-level atom shown in Fig. S1(a) we denote its states as $|i\rangle$ ($i = 1, 2, 3$), with bare energies ξ_i . Clearly, the states $|i\rangle$ are eigenstates of the bare Hamiltonian \hat{H}_0 , i.e., $\hat{H}_0|i\rangle = \xi_i|i\rangle$ and may be defined to form an orthonormal basis: $\langle i|j\rangle$ is 1 if $i = j$ and 0 otherwise. This means that any arbitrary wavefunction for the three-level atom, such as $\Psi(\vec{r}, t)$ in Eqn. 10, may be expressed as a linear superposition of the states $|i\rangle$ with time-dependent weighting coefficients a_i : $\Psi(\vec{r}, t) = \sum_{i=1}^3 a_i(t)|i\rangle$, where $\sum_{i=1}^3 |a_i|^2 = 1$. Substituting this into Eqn. 10, and introducing $\hbar\omega_{ij} \equiv \xi_i - \xi_j$ for $i \neq j$, we project the resultant equation onto each of the $|i\rangle$ -states to obtain

$$\begin{aligned} i\hbar\dot{a}_1 &= V_{13}a_3 \\ i\hbar\dot{a}_2 &= \hbar\omega_{21}a_2 + V_{23}a_3 \\ i\hbar\dot{a}_3 &= \hbar\omega_{31}a_3 + V_{32}a_2 + V_{31}a_1, \end{aligned} \quad (11)$$

where we have put $\xi_1 = 0$. Further, we have assumed that the $1 \leftrightarrow 2$ transition is dipole-forbidden. In Eqns. 11 the interaction symbols V_{ij} are defined as: $V_{ij} = \langle i| -\vec{d}|j\rangle \cdot \vec{E}(t) = -\hat{\vec{d}}_{ij} \cdot \vec{E}$. Note that the V_{ii} terms are zero because the spatial states $|i\rangle$ have well-defined parity and \vec{d} is an odd spatial function. Also note that $\hat{\vec{d}}_{ij}^* = \hat{\vec{d}}_{ji}$ because $\hat{\vec{d}}$ is real.

Assuming the incident field $\hat{\vec{E}}(t)$ to be a sum of the coupling and probe fields each of which is a monochromatic plane-wave of frequency ω_c and ω_p , amplitude E_c and E_p , and polarization unit vectors $\vec{\epsilon}_c$ and $\vec{\epsilon}_p$, we may write

$$\hat{\vec{E}}(t) = \frac{1}{2}\vec{\epsilon}_c E_c e^{-i\omega_c t} + \frac{1}{2}\vec{\epsilon}_p E_p e^{-i\omega_p t} + c.c., \quad (12)$$

where *c.c.* denotes complex conjugate, and we have assumed the atom to be located at the origin for convenience [3]. Substituting Eqn. 12 in Eqns. 11 we find that

$$\begin{aligned} \dot{a}_1 &= \frac{i}{2\hbar} \vec{d}_{13} \cdot (\vec{\epsilon}_p E_p e^{-i\omega_p t} + \vec{\epsilon}_p^* E_p^* e^{i\omega_p t}) a_3 \\ \dot{a}_2 &= -i\omega_{21}a_2 + \frac{i}{2\hbar} \vec{d}_{23} \cdot (\vec{\epsilon}_c E_c e^{-i\omega_c t} + \vec{\epsilon}_c^* E_c^* e^{i\omega_c t}) a_3 \\ \dot{a}_3 &= -i\omega_{31}a_3 + \frac{i}{2\hbar} \vec{d}_{32} \cdot (\vec{\epsilon}_c E_c e^{-i\omega_c t} + \vec{\epsilon}_c^* E_c^* e^{i\omega_c t}) a_2 \\ &\quad + \frac{i}{2\hbar} \vec{d}_{31} \cdot (\vec{\epsilon}_p E_p e^{-i\omega_p t} + \vec{\epsilon}_p^* E_p^* e^{i\omega_p t}) a_1 \end{aligned} \quad (13)$$

In order to solve the differential equations in Eqns. 13, we take a cue from the case of zero incident fields (i.e., $E_p = E_c = 0$), for which the solutions are trivially obtained as $a_1(t) = a_1(0)$, $a_2(t) = a_2(0)e^{-i\omega_{21}t}$, where $\omega_{21} = \omega_{31} - \omega_{32}$, and $a_3(t) = a_3(0)e^{-i\omega_{31}t}$. Next, we guess at the nonzero incident field solutions by simply replacing the constants $a_i(0)$ in the zero-incident field solutions with the slowly-varying coefficients $c_i(t)$ (which are as yet unknown, and must be solved for as shown below), and replacing ω_{31} and ω_{32} by ω_p and ω_c respectively (because we expect the driving frequencies ω_c , ω_p to dominate after long times). This yields

$$\begin{aligned} a_1(t) &= c_1(t) \\ a_2(t) &= c_2(t)e^{-i(\omega_p - \omega_c)t} \\ a_3(t) &= c_3(t)e^{-i\omega_p t} \end{aligned} \quad (14)$$

We now replace the a_i 's in Eqns. 13 with the c_i 's from Eqns. 14, and invoke the rotating wave approximation (RWA) which lets us ignore terms oscillating at twice the optical frequency because they average to zero (measurement times exceed a few optical cycles). We obtain:

$$\begin{aligned}\dot{c}_1 &= i\chi_p^* c_3 \\ \dot{c}_2 &= i(\Delta_c - \Delta_p)c_2 + i\chi_c^* c_3 \\ \dot{c}_3 &= -i\Delta_p c_3 + i\chi_c c_2 + i\chi_p c_1\end{aligned}\quad (15)$$

where we have defined the probe and coupling Rabi frequencies as $\chi_p \equiv \vec{d}_{31} \cdot \vec{\epsilon}_p E_p / 2\hbar$ and $\chi_c \equiv \vec{d}_{32} \cdot \vec{\epsilon}_c E_c / 2\hbar$, respectively. Recall that the Rabi frequency is the rate at which the state-occupation probability of a resonantly excited two-level atom oscillates between the excited and ground states. In writing Eqns. 15 we have introduced the pump and probe detunings $\Delta_c = \omega_{32} - \omega_c$ and $\Delta_p = \omega_{31} - \omega_p$. Further, note that in going from Eqns. 13 to 15 we have used $\vec{d}_{13} \cdot \vec{\epsilon}_p^* E_p^* / 2\hbar = \vec{d}_{31}^* \cdot \vec{\epsilon}_p^* E_p^* / 2\hbar = \chi_p^*$, and a similar argument to derive χ_c^* .

C. Optical Bloch equations

Experiments measure probabilities and coherences. We therefore introduce $\rho_{ii} \equiv c_i c_i^*$ the probability of the atom being in the state $|i\rangle$, and $\rho_{ij} \equiv c_i c_j^*$ the coherence between states $|i\rangle$ and $|j\rangle$. Our task is to convert the “c-dot equations” into differential equations for ρ_{ij} , which are known as the optical Bloch equations.

The ρ_{ij} 's can be expressed as elements of a probability density matrix for light-atom interaction denoted by $\hat{\rho}$. Thus, for an illuminated three-level atom, $\hat{\rho}$ is a 3×3 matrix with diagonal elements ρ_{ii} representing the population in level $|\phi_i\rangle$ and off-diagonal elements ρ_{ij} ($i \neq j$) representing the coherence (or strength or amplitude) of the induced dipole operator \hat{V} between $|i\rangle$ and $|j\rangle$. The use of the word “coherence” here, associated with the product of probability amplitudes for the atom to be in either of two different quantum states can be confusing to students - it may help to consider an analogy to the coherence of an electromagnetic wave which is determined by measuring the product of probability amplitudes for the detected photon to have taken either path in a double-slit experiment (or alternatively, the product of electric field amplitudes for each of the two interfering light fields).

The connection of the off-diagonal terms ρ_{ij} ($i \neq j$) with the induced dipole moment between states $|i\rangle$ and $|j\rangle$ is clearly brought out by directly evaluating the expectation value $\langle \hat{d} \rangle$ of the induced dipole moment operator \hat{d} in the state Ψ . Using Eqn. 14 we obtain $\langle \hat{d} \rangle = \sum_{i=1}^3 (|a_i|^2 \vec{d}_{ii}) + \sum_{i \neq j}^3 (a_i^* a_j \vec{d}_{ij})$, where the first sum does not contribute because the \vec{d}_{ii} 's are zero for the same reason we put $V_{ii} = 0$ earlier (See Sec. S1B above). We find

$$\begin{aligned}\langle \hat{d} \rangle &= \rho_{12} e^{i(\omega_p - \omega_c)t} \vec{d}_{21} + \rho_{13} e^{i\omega_p t} \vec{d}_{31} \\ &\quad + \rho_{23} e^{i\omega_c t} \vec{d}_{32} + c.c.\end{aligned}\quad (16)$$

In order to calculate the probe absorption we should focus our attention on the $\rho_{13} \vec{d}_{31}$ term in Eqn. 16. Clearly ρ_{13} is the weighting coefficient of the induced dipole moment \vec{d}_{31} oscillating at the probe frequency between levels $|1\rangle$ and $|3\rangle$. Extracting this term from Eqn. 16

$$\langle \hat{d} \rangle_{\text{probe}} = \rho_{13} e^{i\omega_p t} \vec{d}_{31} + c.c. \quad (17)$$

from which it is clear our next step is to calculate ρ_{13} .

The optical Bloch equations are deduced from the c-dot equations by using $\dot{\rho}_{ij} = c_i \dot{c}_j^* + \dot{c}_i c_j^*$. In the usual situation the pump is strong and the probe weak causing almost all population to pump into level $|1\rangle$ in Fig. S1(a), meaning that $\rho_{11} \approx 1$ and $\rho_{22} \approx \rho_{33} \approx 0$ (also, $\rho_{32} \approx 0$). In this *weak probe approximation* we find

$$\begin{aligned}\dot{\rho}_{13} &= i\Delta_p \rho_{13} - i\chi_c^* \rho_{12} - i\chi_p^* \\ \dot{\rho}_{12} &= i(\Delta_p - \Delta_c) \rho_{12} - i\chi_c \rho_{13} \\ \dot{\rho}_{23} &\approx 0\end{aligned}\quad (18)$$

We have so far ignored decoherence/relaxation/line-broadening mechanisms - these are discussed in the main article. Elastic collisions, for example, cause an exponential decay of the phase of the induced dipole moments ρ_{12} and ρ_{13} while inelastic collisions cause an exponential decay of their magnitudes [4]. We lump all elastic and inelastic damping processes causing relaxation of the induced dipole moment between $|2\rangle$ and $|1\rangle$ into one term γ_{12} which we call the “ground state decoherence rate”. The same elastic and inelastic damping processes, but now with spontaneous emission added in, cause the induced dipole moment between the excited state $|3\rangle$ and $|1\rangle$ (or $|2\rangle$) to relax at a rate

which we denote as γ_{13} (or γ_{23}). If spontaneous emission is the dominant dephasing mechanism, it is well-known that the coherence decay rate is half that of the population decay rate [4], i.e., we may take $\gamma_{13} = \gamma_{23} = \Gamma/2$, where Γ is the excited state spontaneous emission rate. Including these exponential dephasing terms in Eqns. 18 we obtain

$$\begin{aligned}\dot{\rho}_{13} &= i(\Delta_p + i\gamma_{13})\rho_{13} - i\chi_c^*\rho_{12} - i\chi_p^* \\ \dot{\rho}_{12} &= i(\Delta_p - \Delta_c + i\gamma_{12})\rho_{12} - i\chi_c\rho_{13}\end{aligned}\quad (19)$$

Experiments deal with real atoms that have multiple levels - a limitation of our three-level model is that we consider a “closed” system where we do not account for population leaking to extraneous energy-levels. Even so, the three-level model is widely-used and predicts experimental outcomes, at least qualitatively, surprisingly well.

The most important solutions to Eqns. 19 are “steady-state solutions”, obtained for times $t \gg 1/\gamma_{12}, 1/\gamma_{13}$. In this long-time limit, at times long after the atomic variables have “relaxed” to their steady-state values, ρ_{12} and ρ_{13} are no longer functions of time. Setting $\dot{\rho}_{12}$ and $\dot{\rho}_{13}$ equal to zero, we obtain the steady-state solution:

$$\rho_{13} = \frac{\chi_p^*(\Delta_p - \Delta_c + i\gamma_{12})}{(\Delta_p - \Delta_c + i\gamma_{12})(\Delta_p + i\gamma_{13}) - |\chi_c|^2}. \quad (20)$$

Eqns. 19 and 20 are derived in Ref. [1], except that our equations include nonzero pump detuning Δ_c .

Recall from Eqn. 17 that ρ_{13} is related to the steady-state magnitude of the induced dipole moment at the probe frequency. Hence ρ_{13} has a direct connection to the polarizability of the medium (defined as the induced dipole moment per atom, which we denote by α_p). In the lab, however, we measure probe absorption. Therefore, we need to connect ρ_{13} with probe absorption. For the benefit of undergraduates who may not have had a course in optics, we briefly describe in the next sub-section how we arrive at a well-known relation between the absorption and the polarizability α_p .

D. Absorption, refractive index, polarizability

The absorption and polarizability are related to each other through their connection with the refractive index. We first examine the relation between absorption and refractive index. The simplest description of the attenuation of a light beam as it propagates through a medium (say, a plane wave $\vec{E}(z, t) = \vec{E}_0 e^{i(kz - \omega t)}$ propagating in the z -direction) is given by Beer’s Law: $I(z) = I_0 \exp(-\alpha z)$, where I_0 is the intensity at $z = 0$, and α is the attenuation coefficient. The incident intensity attenuates exponentially due to both scattering and absorption - the latter dominates at near-resonance incident frequencies, in which case we may simply refer to α as the absorption coefficient. The refractive index of the medium n enters through the well-known wave relation $k = n\omega/c$ between the spatial frequency k and temporal frequency ω . In the presence of absorption n becomes complex and we may write the refractive index in terms of real and imaginary parts: $n = n_r + i n_i$. Substituting the resulting complex expression for k into the plane wave amplitude above, we find $\vec{E}(z, t) = \vec{E}_0 e^{-n_i \omega z/c} e^{i(n_r \omega z/c - \omega t)}$, from which we may derive $I(z) = I_0 \exp(-2n_i \omega z/c)$. Comparing this relation with the above mentioned statement of Beer’s Law we arrive at the well-known relation between the absorption coefficient and the imaginary refractive index:

$$\alpha = 2n_i \omega/c. \quad (21)$$

Next, we remind the reader of the well-known relation between the macroscopic refractive index and the polarizability, derived by applying Maxwell’s equations in a linear non-magnetic medium with no free currents:

$$n = \sqrt{1 + N\alpha_p/\epsilon_0} \xrightarrow[n \sim 1]{\text{gas}} 1 + N\alpha_p/2\epsilon_0 \quad (22)$$

Eqn. 22 is arrived at by starting with one of the curl equations, say, $\vec{\nabla} \times \vec{B} = \mu_0 \partial_t (\epsilon_0 \vec{E} + \vec{P})$, where $\partial_t \equiv \partial/\partial t$ and \vec{P} is the electric polarization of the medium (defined as the dipole moment per unit volume), i.e., $\vec{P} = N\alpha_p \vec{E}$ where N is the atomic density, or more precisely, the number of atomic dipoles per unit volume. Taking the curl on both sides of this Maxwell’s equation we obtain $\nabla^2 \vec{E} = \mu_0 \epsilon_0 (1 + N\alpha_p/\epsilon_0) \partial_t^2 \vec{E}$ which, upon comparison with the wave equation $\nabla^2 \vec{E} = (n^2/c^2) \partial_t^2 \vec{E}$, yields the relation $n^2 = 1 + N\alpha_p/\epsilon_0$. For a gas the refractive index $n \sim 1$, and we may apply a binomial approximation to eliminate the square root (see Eqn. 22).

Now, how to calculate the polarizability α_p ? The answer lies in an examination of Eqns. 17 and 20 and the realization that the definition of the polarizability stated in the caption to Fig. S1 allows us to use Eqn. 12 to write:

$$\langle \hat{d} \rangle_{\text{probe}} = \alpha_p \left(\frac{1}{2} \vec{\epsilon}_p E_p e^{-i\omega_p t} + \text{c.c.} \right). \quad (23)$$

Equating terms oscillating at the same frequency in Eqns. 17 and 23, we find

$$\frac{1}{2} \alpha_p \vec{\epsilon}_p E_p = \rho_{31} \vec{d}_{13} \quad (24)$$

which, upon taking the dot product with $\vec{\epsilon}_p^*$ on both sides and using the fact that $\vec{\epsilon}_p \cdot \vec{\epsilon}_p^* = 1$, yields

$$\frac{1}{2}\alpha_p E_p = \rho_{31}\vec{d}_{13} \cdot \vec{\epsilon}_p^* \quad (25)$$

Substituting the complex conjugate of Eqn. 20 in Eqn. 25 we obtain

$$\alpha_p = \frac{|\mu_{13}|^2}{\hbar} \frac{\Delta_p - \Delta_c - i\gamma_{12}}{(\Delta_p - \Delta_c - i\gamma_{12})(\Delta_p - i\gamma_{13}) - |\chi_c|^2} \quad (26)$$

where we have used the definition of χ_p as stated immediately after Eqn. 15, and we have introduced the symbol $\mu_{13} = \vec{d}_{13} \cdot \vec{\epsilon}_p^*$ to denote the projection of the transition dipole moment on the direction of the field polarization (note that $|\mu_{13}|^2$ is directly related to the Clebsch-Gordan coefficient for the probe transition).

We now substitute Eqn. 26 in Eqn. 22. We rationalize the expression for α_p in Eqn. 26, and equate the real and imaginary parts separately in Eqn. 22. Using Eqn. 21, we obtain for the absorption coefficient α :

$$\begin{aligned} \alpha &= \frac{N\omega_p |\mu_{13}|^2}{\epsilon_0 c \hbar} \\ &\times \frac{\gamma_{13}\Delta'^2 + \gamma_{12}(\gamma_{12}\gamma_{13} + |\chi_c|^2)}{[\Delta_p\Delta' - \gamma_{12}\gamma_{13} - |\chi_c|^2]^2 + [\gamma_{12}\Delta_p + \gamma_{13}\Delta']^2} \end{aligned} \quad (27)$$

and for the real part of the refractive index n_r

$$\begin{aligned} n_r &= 1 + \frac{N}{2\epsilon_0} \frac{|\mu_{13}|^2}{\hbar} \\ &\times \frac{\Delta'(\Delta'\Delta_p - |\chi_c|^2) + \gamma_{12}^2\Delta_p}{[\Delta_p\Delta' - \gamma_{12}\gamma_{13} - |\chi_c|^2]^2 + [\gamma_{12}\Delta_p + \gamma_{13}\Delta']^2} \end{aligned} \quad (28)$$

where $\Delta' \equiv$ relative probe-coupling detuning $\Delta_p - \Delta_c$ (also referred to as the Raman detuning).

It is instructive to examine Eqns. 27 and 28 in the limit $\chi_c = 0$ (pump off). Of course, no EIT occurs so we should recover the usual results for absorption and real refractive index. Eqn. 27 for the absorption yields

$$\alpha \xrightarrow{\chi_c=0} \frac{N\omega_p}{\epsilon_0 c} \frac{|\mu_{13}|^2}{\hbar} \frac{\gamma_{13}}{\Delta_p^2 + \gamma_{13}^2} \quad (29)$$

which follows the expected Lorentzian absorptive line shape with half width at half maximum (HWHM) γ_{13} for a stationary atom, attaining its maximum value at $\Delta_p = 0$. Eqn. 29 is depicted in Fig. S2(a) for the ^{87}Rb D1 transition where $2\gamma_{13}/2\pi = 5.75$ MHz [5].

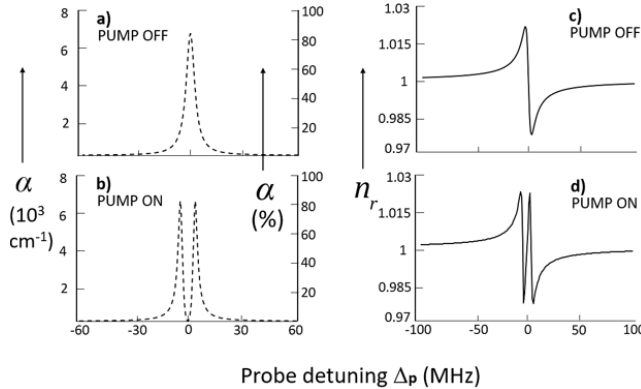


Fig. S2. The absorption coefficient α , depicted by the dashed lines in (a) and (b), and the real refractive index n_r , depicted by the solid lines in (c) and (d), as predicted by Eqns. 27-30. The case of “no pump” ($\chi_c = 0$) is shown in the top panel (Eqns. 29 and 30) as compared to the “EIT case” ($\chi_c \neq 0$) which is shown in the bottom panel (Eqns. 27 and 28). We used plot parameter-values close to conditions in our experiments: For the ^{87}Rb D1 transition $\gamma_{13}/2\pi = \frac{1}{2}(5.75$ MHz), and $\gamma_{12}/2\pi = 3$ KHz; $|\chi_c|/2\pi = 4$ MHz, $\omega_p/2\pi = 3.77 \times 10^{14}$ Hz, $N = 3.36 \times 10^{11}/\text{cm}^3$, $|\mu_{13}| = 2.54 \times 10^{-29}$ Cm, $\Delta_c = 0$.

For the real refractive index we find from Eqn. 28,

$$n_r \xrightarrow{\chi_c=0} 1 + \frac{N}{2\epsilon_0} \frac{|\mu_{13}|^2}{\hbar} \frac{\Delta_p}{\Delta_p^2 + \gamma_{13}^2} \quad (30)$$

which yields the usual dispersive line shape around probe-resonance, again with a HWHM of γ_{13} . Eqn. 30 is depicted in Fig. S2(c).

Recall from Sec. S1B that Δ_p is defined to be positive when the probe is detuned below resonance, and negative above. The decrease in n_r with frequency near resonance, seen in Fig. S2 (c), is the well-known “anomalous refractive index” effect, anomalous because as one may recall from the classic experiment of passing white light through a glass prism, red light deviates the least and blue the most, signifying that in the usual case (i.e., far from resonance) n_r increases with frequency.

E. EIT contrast and line width

When the control field is on ($\chi_c \neq 0$), the absorption α in Eqn. 27 takes the form as plotted in Fig. S2(b). EIT manifests as a dramatic drop in absorption when the coupling and probe beams are in resonance with each other. In order to obtain simplified expressions for the contrast and line width of the EIT transmission window, we set the probe detuning Δ_p equal to zero in Eqn. 27:

$$\alpha \xrightarrow{\Delta_p=0} \alpha_{\chi_c=0} \left[1 - \frac{|\chi_c|^2}{\gamma_{13}} \frac{\gamma_{12} + \frac{|\chi_c|^2}{\gamma_{13}}}{\Delta_c^2 + \left(\gamma_{12} + \frac{|\chi_c|^2}{\gamma_{13}} \right)^2} \right] \quad (31)$$

where $\alpha_{\chi_c=0}$ is obtained by plugging $\Delta_p = 0$ in Eqn. 29. The first term inside the parentheses in Eqn. 31 represents the baseline absorption without EIT, while the second term is the EIT transmission window - the dip in absorption depicted in Fig. S2(b). This dip in absorption is Lorentzian with a full-width-half-maximum given by:

$$\Gamma_{EIT} = 2 \left(\gamma_{12} + \frac{|\chi_c|^2}{\gamma_{13}} \right) \quad (32)$$

The EIT contrast, or amplitude of the transparency window, is denoted by Δa and is simply obtained by setting $\Delta_c = 0$ in the second term of Eqn. 31:

$$\Delta a = \frac{|\chi_c|^2}{\gamma_{13}\gamma_{12} + |\chi_c|^2} \quad (33)$$

However, as explained in the main article, the closed three-level expressions in Eqns. 27 - 33 above, while useful for visualizing the dependence of the EIT linewidth and contrast on various parameters (see Fig. S2), are not useful for making quantitative predictions of the linewidth and contrast actually observed in experiments.

F. Dark and bright states in EIT

In order to better understand the results in Sec. S1 E above, we ask the question: What are the new eigenstates and eigenenergies for the Hamiltonian in Eqn. 10 describing the three-level atomic system in Fig. S1(a) under illumination by the coupling and probe fields?

To address this question it is advantageous to know the Hamiltonian in matrix form, under the rotating wave approximation and long wavelength approximation, denoted here by \hat{H}_{RWA} . In order to do this using the optical Bloch equations already derived in Sec. S1 C we begin by casting the Schrodinger equation (Eqn. 10) in terms of the density matrix $\hat{\rho}$. We have

$$i\hbar\dot{\hat{\rho}} = [\hat{H}_{RWA}, \hat{\rho}], \quad (34)$$

where $\hat{\rho}$ and \hat{H}_{RWA} are Hermitian matrices, of order 3×3 for the three-level system, each with nine matrix elements of the form ρ_{ij} and H_{ij} (where $i, j = 1, 2, 3$). For the purpose of this sub-section it is convenient to ignore all damping and decoherence processes such as spontaneous emission, collisions, etc. From Eqn. 18 we see that we know all the matrix elements for $\dot{\hat{\rho}}$ already, and can use them to re-construct the Hamiltonian \hat{H}_{RWA} . For example, from Eqn. 34, the matrix elements $i\hbar\rho_{12}$ and $i\hbar\rho_{13}$ are, respectively,

$$\begin{aligned} [\hat{H}_{RWA}, \hat{\rho}]_{12} &= -H_{22}\rho_{12} - H_{12} - H_{32}\rho_{13} \\ [\hat{H}_{RWA}, \hat{\rho}]_{13} &= -H_{33}\rho_{13} - H_{13} - H_{23}\rho_{12} \end{aligned} \quad (35)$$

where we have used the weak-probe approximation $\rho_{32} \approx 0$, $\rho_{22} \approx 0$, and $\rho_{11} \approx 1$ as discussed earlier in Sec. S1C, and we also used $H_{11} = 0$. Comparing the coefficients of the ρ_{12} and ρ_{13} terms in Eqns. 35 and 18, we find

$$H_{RWA} = \hbar \begin{bmatrix} 0 & 0 & -\chi_p^* \\ 0 & -(\Delta_c - \Delta_p) & -\chi_c^* \\ -\chi_p & -\chi_c & \Delta_p \end{bmatrix} \quad (36)$$

Setting the pump and probe detunings equal to zero for simplicity, we find the three eigenvalues for the Hamiltonian in Eqn. 36 to be:

$$(\lambda_0, \lambda_{\pm}) = (0, \pm \hbar\Omega) \quad (37)$$

where Ω is a generalized Rabi frequency defined in terms of the sum of the squares of the pump and probe Rabi frequencies: $\Omega \equiv \sqrt{|\chi_c|^2 + |\chi_p|^2}$. The three orthonormal eigenstates corresponding to these eigenvalues are:

$$\begin{aligned} |0\rangle &= \frac{1}{\Omega} (\chi_c|1\rangle - \chi_p|2\rangle) \\ |\pm\rangle &= \frac{1}{\sqrt{2}} \left(\frac{\chi_p^*|1\rangle + \chi_c^*|2\rangle}{\Omega} \mp |3\rangle \right) \end{aligned} \quad (38)$$

Two revealing insights are obtained from Eqns. 38. First, an atom that happens to be in eigenstate $|0\rangle$ has no overlap with state $|3\rangle$, hence can never excite into state $|3\rangle$. For this reason we refer to $|0\rangle$ as a *dark state*. Note that, in the weak probe approximation ($\chi_p \ll \chi_c$) we find that $|0\rangle \approx |1\rangle$. Second, if we re-cast the two non-dark states $|\pm\rangle$ in Eqn. 38 in terms of two new *non-stationary* states $|+\rangle$ and $|-\rangle$:

$$|\pm'\rangle = \frac{1}{\sqrt{2}} (|-\rangle \pm |+)\rangle \quad (39)$$

we see that, in the weak probe approximation, $|+\rangle \approx |2\rangle$ and $|-\rangle \approx |3\rangle$. Here, $|+\rangle$ and $|-\rangle$ are not stationary states because the strong coupling field oscillates the atoms back and forth between $|+\rangle \approx |2\rangle$ and $|-\rangle \approx |3\rangle$. We therefore refer to the $|+\rangle$ -state, which is strongly coupled to $|3\rangle$, as the *bright state*. Thus, the corollary is that in the weak probe approximation, we may think of states $|1\rangle$ and $|2\rangle$ in our three-level system (see Fig. S1(a)) as the dark state and bright state, respectively.

Note that atoms in the bright state soon get optically pumped into the dark state where they stay. However, as indicated in the main article, our simple “closed” three-level model for a single atom does not adequately replicate the dense samples of moving atoms with multiple levels that are used in our experiments, and this transfer to the dark state is reduced, leading to significantly reduced EIT contrast.

G. Slow light

The entire discussion in Sec. S1 E above was centered around probe absorption α (Eqn. 27) in the presence of a coupling field - in this sub-section we focus on the real refractive index n_r (Eqn. 28) which is plotted in Fig. S2(d). Slow light arises from the dramatic change in refractive index n_r within the narrow EIT transparency window where the coupling (i.e., pump) and probe beams are in resonance with each other.

The steep gradient of n_r at zero pump-probe detuning significantly impacts the group velocity of light v_g :

$$v_g(\omega_p) \equiv \frac{c}{n_r + \omega_p dn_r/d\omega_p} \quad (40)$$

In particular a steep *positive* gradient about zero detuning, as depicted in Fig. S2, leads to a significantly reduced group velocity. This is elucidated by putting $\Delta_c = 0$ for simplicity in Eqn. 28 and considering the case of strong coupling intensity, i.e.,

$$|\chi_c|^2 \gg \Delta_p^2, \gamma_{12}^2, \gamma_{12}\gamma_{13}, |\Delta_p|\gamma_{13}, \quad (41)$$

to find

$$n_r = 1 - \frac{N}{2\epsilon_0\hbar} \frac{|\mu_{13}|^2}{|\chi_c|^2} \Delta_p. \quad (42)$$

Substituting Eqn. 42 in Eqn. 40, and recalling that $\Delta_p \equiv \omega_{31} - \omega_p$, we obtain for the group velocity

$$\frac{v_g}{c} \approx \frac{|\chi_c|^2}{|\chi_c|^2 + \frac{N|\mu_{13}|^2}{2\epsilon_0\hbar} \omega_p}. \quad (43)$$

If we choose the coupling intensity such that we satisfy:

$$|\chi_c|^2 \ll \frac{N|\mu_{13}|^2}{2\epsilon_0\hbar} \omega_p \quad (44)$$

we can make $v_g/c \ll 1$, thus achieving slow light.

As explained in the main article, the conditions in Eqns. 41 and 44 are always satisfied in our experiments.

S2. Rubidium hyperfine structure

Our experiments are performed on the D1 transition $5^2S_{1/2}, F_g = 2 \rightarrow 5^2P_{1/2}, F_e = 1$ in ^{87}Rb atomic gas. Among the alkali elements Rubidium is popular owing to the ready availability of inexpensive user-friendly commercial diode lasers at the resonance wavelength for transitions from the $5^2S_{1/2}$ ground state to either the $5^2P_{1/2}$ excited state (D1-transition; 795 nm) or the $5^2P_{3/2}$ excited state (D2-transition; 780 nm). Fig. S3 shows hyperfine energy-levels for both stable isotopes ^{85}Rb (nuclear spin $I = 5/2$) and ^{87}Rb ($I = 7/2$) [5].

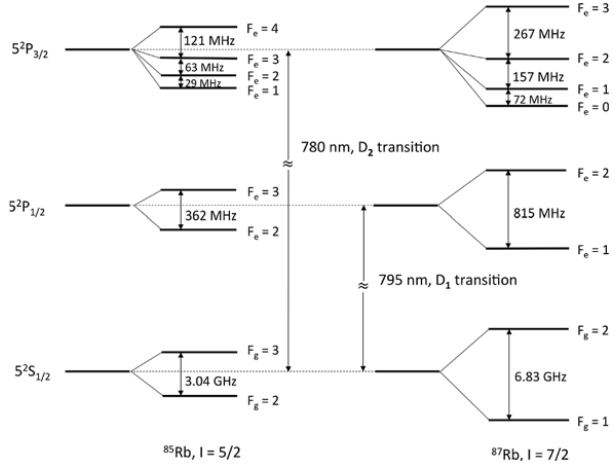


Fig. S3. Rb energy-levels. When we account for electron spin-orbit interaction, the hydrogenic states $5S$ and $5P$ are converted to $5S_{1/2}$ and $5P_{1/2}, 5P_{3/2}$ energy-levels - this is the *fine structure*. The interaction between electron angular momentum and nuclear spin yields the *hyperfine structure*, denoted by the F -quantum numbers. A weak magnetic field causes Zeeman splitting of each of these F -levels into $2m_F + 1$ magnetic sub-levels with quantum numbers $-m_F, -m_F + 1, \dots, m_F - 1, m_F$ (not shown).

As shown in Fig. S3, the hyperfine D1 structure for ^{87}Rb consists of the $5^2S_{1/2}$ ground state and the $5^2P_{1/2}$ excited state, which are split by the interaction of the valence electron's total angular momentum (orbital + spin) with the nuclear spin, creating $F_g = 1, 2$ ground energy states (separated by 6.8 GHz), and $F_e = 1, 2$ excited energy states (separated by 815 MHz), respectively. Each hyperfine state F has $2F + 1$ degenerate substates with quantum number m ranging from $m = -F$ to F in increments of 1. A measurement will find the atom to have an angular momentum component $m\hbar$ along any chosen quantization axis - we choose the z -axis as our axis of quantization. For, say the $F_g = 2$ ground state, the five magnetic substates are revealed in the presence of a weak external magnetic field B_z along the z -axis which removes the degeneracy by imparting the well-known Zeeman shift: $\Delta E = g_f \mu_B m_{F_g} B_z$ to each magnetic sub-level, where g_f is the Lande g-factor for the atomic hyperfine state (1/2 for the $F_g = 2$ ground state), μ_B is the Bohr magneton (9.274×10^{-28} Joules/Gauss), B_z is the external magnetic field magnitude in Gauss and m_{F_g} is the magnetic sub-level number. The Zeeman shifts between the magnetic sub-levels of the $F_g = 2$ ground state are 0.7 KHz/mG [5].

S3. Suppression of stray magnetic fields

In this section we describe in detail how to suppress below 0.2 mG any stray magnetic fields in the laser-atom interaction region. The mu-metal shields need to be frequently de-gaussed using a procedure described below. Further, we describe below a reliable accurate method that is needed to measure the total stray residual magnetic field at levels well below 0.5 mG (less than 1% of the Zeeman field B_z) in the laser-atom interaction region. Typical high-end commercial gauss meters are reliable for measuring magnetic fields down to 10-20 mG, but not below.

A. Degaussing the magnetic shields

The mu-metal sheets lose shielding effectiveness over a period of a few days, primarily owing to mechanical stress created by removing and replacing the end-caps on the triple-shield in order to make changes in the optical setup inside. This is attributed to atomic dipoles becoming progressively magnetically locked together through their own interactions rather than external fields. Therefore, we degaussed the shields just before taking data.

In order to degauss the shields we subject the mu-metal to a large AC magnetic field and slowly lower the strength down to zero. The large AC field will overcome the locked dipoles, forcing their alignment with the AC field. In our experiments, we use a cable wound around the layer of thermal foam (see Fig. 5 in main article) surrounding the inner most mu metal shield to supply the degaussing current. There are ~ 80 turns over a length of ~ 20 cm.

The appropriate rate of decreasing the current is determined empirically. If not decreased optimally, residual fields continue to circulate in the innermost shield which can be detected, as discussed in Sec. S3 B below. By repeatedly modifying and iterating the degaussing process to optimally suppress the residual field we determined an adequate degaussing procedure: We passed a peak current of 5 A through the cable which is slowly lowered over 1-2 minutes using a variac; the current is reduced twice as slowly when under 200 mA.

B. Residual magnetic field measurements

In this sub-section we discuss how to measure residual stray magnetic fields in the entire laser-atom interaction volume - a cylinder of diameter equal to that of the probe beam and length equal to that of the vapor cell - by using a dedicated auxiliary optical pumping technique [6]. We reduce the total stray residual magnetic field well below 0.5 mG (less than 1% of the Zeeman field B_z) as shown below.

To elucidate slow light investigations based on Zeeman EIT we rely upon a well-defined quantization axis (the z -axis), which in our case is collinear with the weak external constant magnetic field B_z and the propagation direction of the pump and probe laser beams. B_z creates Zeeman sub-levels, for each of which the magnetic dipole moment precesses around B_z with an angular momentum component $m\hbar$ along the z -axis. For this choice of quantization axis, if the electric field vector of the incident light field is perpendicular to the z -axis, as is the case for our pump and probe beams, the induced (i.e., absorptive and stimulated) transitions among the Zeeman sub-levels obey the selection rule $\Delta m = \pm 1$ [7]. In other words, the absorption depends upon the projections of the precessing magnetic dipoles along the z -axis. Spontaneous emission from the excited Zeeman states is not associated with any special quantization axis and is constrained only by the selection rule $\Delta m = 0, \pm 1$.

Therefore, any small departure from collinearity between the laser propagation direction and the applied longitudinal magnetic field results in a small component of the strong pump beam (and the weak probe beam too, which we may neglect compared to the pump) causing a persistent undesired $\Delta m = 0$ cycling of some atoms between the $m_{F_g} = 1$ and $m_{F_e} = 1$ levels in Fig. 3(b) in the main article. This weakens our approximation to a three-level lambda scheme, decreasing EIT contrast and broadening EIT linewidth, thus significantly reducing slow light effects.

Assuming the presence of a residual magnetic field pointing along some arbitrary direction, and setting the solenoid current equal to zero, we illuminate the atoms with a single strong circularly-polarized beam, say a σ^+ beam in Fig. 3(b) in the main article, propagating along the z -direction (still the quantization axis), tuned to the $F_g = 2 \rightarrow F_e = 1$ transition. The σ^+ beam intensity I is strong enough ($I > I_{sat}$), and illuminates the atoms for long enough, that a substantial number of atoms is optically pumped into the $F_g = 2, m_{F_g} = +1, +2$ magnetic sub-levels. Turning the strong laser beam off at this point allows the “spin polarization” of the sample to decay, until the population is distributed evenly among the $F_g = 2$ magnetic sub-levels. Note that the transition strengths are different for each specific Δm -transition. Thus sample absorption changes appreciably as the spin polarization decays from strongly polarized to unpolarized.

However, during this depolarization process, the presence of a weak non-axial magnetic field means that the total magnetic field \vec{B} is not aligned with the z -axis. The atomic magnetic dipoles precess around \vec{B} at the Larmor frequency ν_L , given by $h\nu_L = g_f\mu_B|\vec{B}|$. The constants g_f and μ_B are the Lande g-factor and Bohr magneton, respectively, and are provided in Sec. S1 above. The projections on the z -axis of the magnetic dipoles precessing around \vec{B} oscillate at the Larmor frequency, leading to observable oscillations in the sample absorption at ν_L . By measuring the oscillation frequency of spin depolarization with a weak σ^+ probe beam ($I \ll I_{sat}$), we can determine the magnitude of the weak stray B -field from the expression for the Larmor frequency above.

To perform this measurement with best signal-to-noise ratio we create as many spin-polarized atoms as possible by using the vapor cell with higher buffer gas pressure (30 Torr) mentioned in Sec. 5B of the main article, warmed to 65°C to push the number density up to $3.8 \times 10^{11}/\text{cm}^3$ (see Fig. 7(a) in the main article). As outlined in Sec. 3B of the main article, the buffer gas helps suppress rapid spin depolarization due to collisions and transit time effects. We illuminate the atoms with a single circularly polarized beam for which the intensity is square-wave-modulated between two states: A high-intensity state (the pump phase), in which the beam is intense (4.3 mW/cm² in our case) for a period of 500 ms, followed by a low-intensity state (the probe phase) where the beam intensity is kept at

0.044 mW/cm². The low-intensity state is 500 ms long too, though only the first 50 ms need to be recorded. The switching-time between the two intensity-states is 15 μ s. Clear oscillations in the absorption are visible, as shown in Fig. S4(a) for the case of a residual stray magnetic field of 139 μ G.

Fig. S4(b) shows that the application of a small axial magnetic field (here, $B_z = 2.4$ mG) suffices to cause the magnetic dipoles to precess around the z -axis, in which case the projection of each dipole moment along the z -axis ceases to oscillate. The sample is optically pumped toward the $F_g = 2, m_{F_g} = +1, +2$ magnetic sub-levels by the σ^+ -pump, therefore the absorption smoothly increases as the sample becomes spin-polarized.

The inset in Fig. S4(a) shows that this stray B -field measurement technique can be used to optimize the mu-metal shield degaussing procedure. In the example shown, persistent currents in the innermost shield lead to detectable Larmor oscillations in the absorption, corresponding to a residual non-axial magnetic field nearly twice the strength of the typical case depicted in the main plot in Fig. S4(a).

References

1. P. W. Milonni and J. H. Eberly, “Laser Physics”, Wiley (2010), Sec. 9.10, pp 441 - 446
2. This can be seen by considering the Lorentz force in Gaussian units: $\vec{F} = e(\vec{E} + \vec{v}/c \times \vec{B})$, where \vec{E} and \vec{B} have the same dimensions. The second term is negligible when $v \ll c$.
3. For a spatially extended sample illuminated by a *plane* electromagnetic wave propagating in the z -direction, the field $\hat{\vec{E}}$ incident on an atom located at z has a spatial phase e^{ikz} . This spatial phase can be included in the Rabi frequency which is defined immediately after Eqn. 15. However, note that the result for the polarizability α_p in Eqn. 26 depends only on $|\chi_c|^2$, i.e., α_p is the same for all the atoms in the sample. Hence, it is justified to use Eqn. 26 in the macroscopic expression Eqn. 22 in order to obtain Eqns. 27 and 28.
4. See Sec. 9.4 in Ref. [1] for a nice description of how to include relaxation processes in the density matrix.
5. <https://steck.us/alkalidata/>, “Rubidium 85 D line data” and “Rubidium 87 D line data”, by Daniel Steck, University of Oregon
6. M. Shuker, “Decay processes in EIT medium”, PhD thesis, Technion - Israel Institute of Technology (2008)
7. On the other hand, if the electric field vector of the incident light field is along the z -axis, the induced transitions among the Zeeman sub-levels obey the selection rule $\Delta m = 0$, even though the pump and probe beams are ostensibly prepared in Sec. 4B of the main article as σ^+ and σ^- beams.

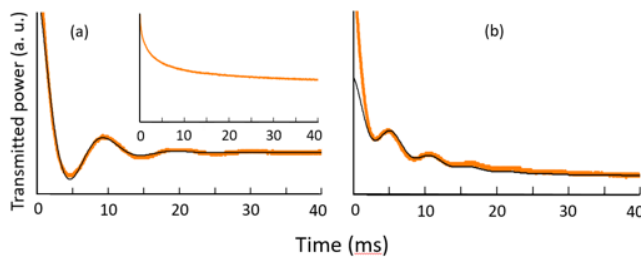


Fig. S4. a) Setting the solenoid current to zero, we can measure the total stray magnetic field by observation of oscillations in the absorption at the Larmor precession frequency, which is determined by fitting with a decaying oscillatory function. Using the equation connecting Larmor frequency to magnetic field (see text), we find a total stray field of 139 μ G in a typical measurement. The inset shows that by turning on a small solenoid current, the application of a small axial magnetic field, 2.4 mG in this case, is sufficient to cause the Larmor oscillations in absorption to disappear. b) If the de-gaussing procedure is not optimized, the same measurement typically yields a significantly higher stray residual magnetic field, 244 μ G in this case.

SUPPLEMENTARY NOTES

Producing slow light in warm alkali vapor using electromagnetically induced transparency

Compiled March 18, 2022

In order to complement the undergraduate-friendly detailed experimental description in the main article, here we provide a detailed theoretical description of the basic physics behind slow light using electromagnetically induced transparency (EIT). In the sections below we follow closely the excellent treatment in Ref. [1], but include non-zero pump laser detuning, and a section on dark and bright states. We endeavor to keep the discussion amenable to advanced juniors and seniors. We include a background section on the atomic hyperfine structure of ^{87}Rb , and a final section on details of an auxiliary measurement to ensure that residual stray magnetic fields are suppressed below 0.2 milliGauss. © 2022 Optical Society of America

1. Theoretical Background

The theoretical discussion of EIT and slow light centers around calculating the complex refractive index $n = n_r + in_i$ of the medium. The imaginary part n_i yields the absorption spectrum where EIT in atomic media is revealed as a narrow transparency window near resonance. The real part n_r yields the group velocity of light propagating through the medium. Slow light is revealed as a consequence of the steep frequency-variation of n_r within the EIT transparency window.

We begin by defining a three-level system, the simplest atomic energy-level configuration in which to elucidate the basic concepts of EIT and slow light. Next, we write down the Hamiltonian and the Schrodinger equation for this system, and derive the widely used optical Bloch equations. These equations are used to calculate the complex refractive index n of the gaseous sample, and reveal the required conditions for EIT and slow light.

A. Three-level system for EIT and slow light

Following the notation in Ref. [1] we depict a fictitious three-level atomic model in Fig. 1(a), in which transitions are allowed between states 1 and 3 and between states 2 and 3 but not between states 1 and 2. The standard EIT experiment consists of a strong coupling (or pump) beam of frequency ω_c and a weak probe beam of frequency ω_p , both tuned to near-resonance with $|3\rangle$ from levels $|2\rangle$ and $|1\rangle$ respectively, with detunings Δ_c and Δ_p . We assume that the pump beam only addresses the coupling transition $|2\rangle \rightarrow |3\rangle$ and the probe beam only addresses the $|1\rangle \rightarrow |3\rangle$ transition. The probe frequency is scanned around the (fixed) pump frequency, and the probe transmission spectrum is measured.

B. Hamiltonian for light-atom interaction

If we denote the wavefunction for the atom interacting with an incident light field as $\Psi(\vec{r}, t)$, the time evolution of Ψ is described by the Schrödinger equation

$$i\hbar \frac{\partial \Psi(\vec{r}, t)}{\partial t} = \hat{H}\Psi(\vec{r}, t) = (\hat{H}_0 + \hat{V})\Psi(\vec{r}, t). \quad (1)$$

Here, \hat{H} is the Hamiltonian for the system, i.e., the energy operator (potential plus kinetic) of the system, act-

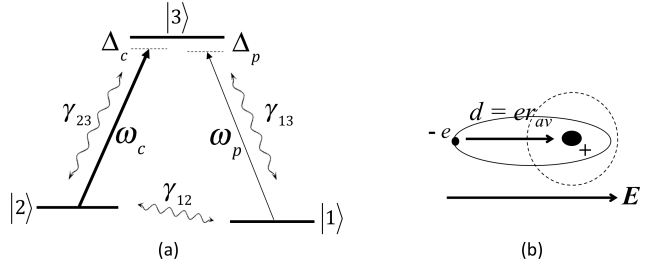


Fig. 1. a) Three-level atomic model. A strong coupling (or pump) beam of frequency ω_c and a weak probe beam of frequency ω_p , are both tuned to near-resonance with $|3\rangle$ from levels $|2\rangle$ and $|1\rangle$ respectively, with detunings Δ_c and Δ_p . Decoherence rates between levels 3 and 1, 3 and 2, 2 and 1, are denoted by γ_{13} , γ_{23} , γ_{12} , respectively (see Eqns. 10 and preceding text). b) Depiction of an atom showing a lone valence electron orbiting the nucleus (big dot). In the absence of an external field, the mean dipole moment, averaged over an electron revolution (circular orbit), is zero. When illuminated by an electric field \vec{E} , the electron cloud shifts in the opposite direction (elliptical orbit) creating an induced dipole moment \vec{d} of magnitude er_{av} , where $r_{av} (\propto E)$ represents the average displacement between the positive and negative regions of the atom. The polarizability α_p is defined by $\vec{d} = \alpha_p \vec{E}$.

ing upon the wavefunction Ψ . Since we are focusing on just the atom and its interaction with the incident field, we may ignore the contribution to the Hamiltonian from the incident field alone (also known as the free field). In that case it is convenient to express the Hamiltonian operator \hat{H} as a sum of two terms, where \hat{H}_0 is the bare Hamiltonian which describes the atom in the absence of any external field, and \hat{V} is the interaction Hamiltonian which describes the interaction between the atom and the external field.

Typically the outermost electrons of the atom are the least tightly bound and respond most readily to the incident field. Indeed, this is an important reason why alkali atoms are favorites with physicists - relatively low optical energies are needed to resonantly excite the lone valence electron. Further, the interaction of the single elec-

tron with the incident field is simple to model. The incident electromagnetic field's electric and magnetic vectors, $\vec{E}(\vec{r}, t)$ and $\vec{B}(\vec{r}, t)$ respectively, interact with the valence electron (negative charge e) through the Lorentz force. The electron speed is typically non-relativistic, so the effect of the \vec{B} -field may be ignored [2]. The $e\vec{E}$ -term in the Lorentz force induces an electric dipole \vec{d} in the atom (see Fig. 1(b)).

Thus, \hat{V} is given by the potential energy stored in this induced dipole, $\hat{V} = -\hat{\vec{d}} \cdot \hat{\vec{E}}(\vec{r}, t)$ where \vec{r} is simply the location of the atomic center of mass. We ignore the variation of \vec{E} over the spatial extent of the atom (typically 0.1 - 1 nm) because the optical wavelength (typically hundreds of nm) is much larger.

For the simple three-level atom shown in Fig. 1(a) we denote its states as $|i\rangle$ ($i = 1, 2, 3$), with bare energies ξ_i . Clearly, the states $|i\rangle$ are eigenstates of the bare Hamiltonian \hat{H}_0 , i.e., $\hat{H}_0|i\rangle = \xi_i|i\rangle$ and may be defined to form an orthonormal basis: $\langle i|j\rangle$ is 1 if $i = j$ and 0 otherwise. This means that any arbitrary wavefunction for the three-level atom, such as $\Psi(\vec{r}, t)$ in Eqn. 1, may be expressed as a linear superposition of the states $|i\rangle$ with time-dependent weighting coefficients

$$a_i: \Psi(\vec{r}, t) = \sum_{i=1}^3 a_i(t)|i\rangle, \text{ where } \sum_{i=1}^3 |a_i|^2 = 1. \text{ Substituting this into Eqn. 1, and introducing } \hbar\omega_{ij} \equiv \xi_i - \xi_j \text{ for } i \neq j, \text{ we project the resultant equation onto each of the } \langle i| \text{-states to obtain}$$

$$\begin{aligned} i\hbar\dot{a}_1 &= V_{13}a_3 \\ i\hbar\dot{a}_2 &= \hbar\omega_{21}a_2 + V_{23}a_3 \\ i\hbar\dot{a}_3 &= \hbar\omega_{31}a_3 + V_{32}a_2 + V_{31}a_1, \end{aligned} \quad (2)$$

where we have put $\xi_1 = 0$. Further, we have assumed that the $1 \leftrightarrow 2$ transition is dipole-forbidden. In Eqns. 2 the interaction symbols V_{ij} are defined as: $V_{ij} = \langle i| - \hat{\vec{d}}|j\rangle \cdot \vec{E}(t) = -\hat{\vec{d}}_{ij} \cdot \vec{E}$. Note that the V_{ii} terms are zero because the spatial states $|i\rangle$ have well-defined parity and \vec{d} is an odd spatial function. Also note that $\hat{\vec{d}}_{ij}^* = \hat{\vec{d}}_{ji}$ because $\hat{\vec{d}}$ is real.

Assuming the incident field $\hat{\vec{E}}(t)$ to be a sum of the coupling and probe fields each of which is a monochromatic plane-wave of frequency ω_c and ω_p , amplitude E_c and E_p , and polarization unit vectors $\vec{\epsilon}_c$ and $\vec{\epsilon}_p$, we may write

$$\hat{\vec{E}}(t) = \frac{1}{2}\vec{\epsilon}_c E_c e^{-i\omega_c t} + \frac{1}{2}\vec{\epsilon}_p E_p e^{-i\omega_p t} + c.c., \quad (3)$$

where *c.c.* denotes complex conjugate, and we have assumed the atom to be located at the origin for convenience [3]. Substituting Eqn. 3 in Eqns. 2 we find that

$$\begin{aligned} \dot{a}_1 &= \frac{i}{2\hbar}\vec{d}_{13} \cdot (\vec{\epsilon}_p E_p e^{-i\omega_p t} + \vec{\epsilon}_p^* E_p^* e^{i\omega_p t}) a_3 \\ \dot{a}_2 &= -i\omega_{21}a_2 + \frac{i}{2\hbar}\vec{d}_{23} \cdot (\vec{\epsilon}_c E_c e^{-i\omega_c t} + \vec{\epsilon}_c^* E_c^* e^{i\omega_c t}) a_3 \\ \dot{a}_3 &= -i\omega_{31}a_3 + \frac{i}{2\hbar}\vec{d}_{32} \cdot (\vec{\epsilon}_c E_c e^{-i\omega_c t} + \vec{\epsilon}_c^* E_c^* e^{i\omega_c t}) a_2 \\ &\quad + \frac{i}{2\hbar}\vec{d}_{31} \cdot (\vec{\epsilon}_p E_p e^{-i\omega_p t} + \vec{\epsilon}_p^* E_p^* e^{i\omega_p t}) a_1 \end{aligned} \quad (4)$$

In order to solve the differential equations in Eqns. 4, we take a cue from the case of zero incident fields (i.e., $E_p = E_c = 0$), for which the solutions are trivially obtained as $a_1(t) = a_1(0)$, $a_2(t) = a_2(0)e^{-i\omega_{21}t}$, where $\omega_{21} = \omega_{31} - \omega_{32}$, and $a_3(t) = a_3(0)e^{-i\omega_{31}t}$. Next, we guess at the nonzero incident field solutions by simply replacing the constants $a_i(0)$ in the zero-incident field solutions with the slowly-varying coefficients $c_i(t)$ (which are as yet unknown, and must be solved for as shown below), and replacing ω_{31} and ω_{32} by ω_p and ω_c respectively (because we expect the driving frequencies ω_c , ω_p to dominate after long times). This yields

$$\begin{aligned} a_1(t) &= c_1(t) \\ a_2(t) &= c_2(t)e^{-i(\omega_p - \omega_c)t} \\ a_3(t) &= c_3(t)e^{-i\omega_p t} \end{aligned} \quad (5)$$

We now replace the a_i 's in Eqns. 4 with the c_i 's from Eqns. 5, and invoke the rotating wave approximation (RWA) which lets us ignore terms oscillating at twice the optical frequency because they average to zero (measurement times exceed a few optical cycles). We obtain:

$$\begin{aligned} \dot{c}_1 &= i\chi_p^* c_3 \\ \dot{c}_2 &= i(\Delta_c - \Delta_p)c_2 + i\chi_c^* c_3 \\ \dot{c}_3 &= -i\Delta_p c_3 + i\chi_c c_2 + i\chi_p c_1 \end{aligned} \quad (6)$$

where we have defined the probe and coupling Rabi frequencies as $\chi_p \equiv \vec{d}_{31} \cdot \vec{\epsilon}_p E_p / 2\hbar$ and $\chi_c \equiv \vec{d}_{32} \cdot \vec{\epsilon}_c E_c / 2\hbar$, respectively. Recall that the Rabi frequency is the rate at which the state-occupation probability of a resonantly excited two-level atom oscillates between the excited and ground states. In writing Eqns. 6 we have introduced the pump and probe detunings $\Delta_c = \omega_{32} - \omega_c$ and $\Delta_p = \omega_{31} - \omega_p$. Further, note that in going from Eqns. 4 to 6 we have used $\vec{d}_{13} \cdot \vec{\epsilon}_p^* E_p^* / 2\hbar = \vec{d}_{31}^* \cdot \vec{\epsilon}_p^* E_p^* / 2\hbar = \chi_p^*$, and a similar argument to derive χ_c^* .

C. Optical Bloch equations

Experiments measure probabilities and coherences. We therefore introduce $\rho_{ii} \equiv c_i c_i^*$ the probability of the atom being in the state $|i\rangle$, and $\rho_{ij} \equiv c_i c_j^*$ the coherence between states $|i\rangle$ and $|j\rangle$. Our task is to convert the “c-dot equations” into differential equations for ρ_{ij} , which are known as the optical Bloch equations.

The ρ_{ij} 's can be expressed as elements of a probability density matrix for light-atom interaction denoted by

$\hat{\rho}$. Thus, for an illuminated three-level atom, $\hat{\rho}$ is a 3×3 matrix with diagonal elements ρ_{ii} representing the population in level $|i\rangle$ and off-diagonal elements ρ_{ij} ($i \neq j$) representing the coherence (or strength or amplitude) of the induced dipole operator \hat{V} between $|i\rangle$ and $|j\rangle$. The use of the word “coherence” here, associated with the product of probability amplitudes for the atom to be in either of two different quantum states can be confusing to students - it may help to consider an analogy to the coherence of an electromagnetic wave which is determined by measuring the product of probability amplitudes for the detected photon to have taken either path in a double-slit experiment (or alternatively, the product of electric field amplitudes for each of the two interfering light fields).

The connection of the off-diagonal terms ρ_{ij} ($i \neq j$) with the induced dipole moment between states $|i\rangle$ and $|j\rangle$ is clearly brought out by directly evaluating the expectation value $\langle \hat{d} \rangle$ of the induced dipole moment operator \hat{d} in the state Ψ . Using Eqn. 5 we obtain $\langle \hat{d} \rangle = \sum_{i=1}^3 (|a_i|^2 \vec{d}_{ii}) + \sum_{i \neq j}^3 (a_i^* a_j \vec{d}_{ij})$, where the first sum does not contribute because the \vec{d}_{ii} ’s are zero for the same reason we put $V_{ii} = 0$ earlier (See Sec. 1B above). We find

$$\begin{aligned} \langle \hat{d} \rangle &= \rho_{12} e^{i(\omega_p - \omega_c)t} \vec{d}_{21} + \rho_{13} e^{i\omega_p t} \vec{d}_{31} \\ &\quad + \rho_{23} e^{i\omega_c t} \vec{d}_{32} + c.c. \end{aligned} \quad (7)$$

In order to calculate the probe absorption we should focus our attention on the $\rho_{13} \vec{d}_{31}$ term in Eqn. 7. Clearly ρ_{13} is the weighting coefficient of the induced dipole moment \vec{d}_{31} oscillating at the probe frequency between levels $|1\rangle$ and $|3\rangle$. Extracting this term from Eqn. 7

$$\langle \hat{d} \rangle_{\text{probe}} = \rho_{13} e^{i\omega_p t} \vec{d}_{31} + c.c. \quad (8)$$

from which it is clear our next step is to calculate ρ_{13} .

The optical Bloch equations are deduced from the c-dot equations by using $\dot{\rho}_{ij} = c_i \dot{c}_j^* + \dot{c}_i c_j^*$. In the usual situation the pump is strong and the probe weak causing almost all population to pump into level $|1\rangle$ in Fig. 1(a), meaning that $\rho_{11} \approx 1$ and $\rho_{22} \approx \rho_{33} \approx 0$ (also, $\rho_{32} \approx 0$). In this *weak probe approximation* we find

$$\begin{aligned} \dot{\rho}_{13} &= i\Delta_p \rho_{13} - i\chi_c^* \rho_{12} - i\chi_p^* \\ \dot{\rho}_{12} &= i(\Delta_p - \Delta_c) \rho_{12} - i\chi_c \rho_{13} \\ \dot{\rho}_{23} &\approx 0 \end{aligned} \quad (9)$$

We have so far ignored decoherence/relaxation/line-broadening mechanisms - these are discussed in the main article. Elastic collisions, for example, cause an exponential decay of the phase of the induced dipole moments ρ_{12} and ρ_{13} while inelastic collisions cause an exponential decay of their magnitudes [4]. We lump all elastic and inelastic damping processes causing relaxation of the induced dipole moment between $|2\rangle$ and $|1\rangle$ into one term

γ_{12} which we call the “ground state decoherence rate”. The same elastic and inelastic damping processes, but now with spontaneous emission added in, cause the induced dipole moment between the excited state $|3\rangle$ and $|1\rangle$ (or $|2\rangle$) to relax at a rate which we denote as γ_{13} (or γ_{23}). If spontaneous emission is the dominant dephasing mechanism, it is well-known that the coherence decay rate is half that of the population decay rate [4], i.e., we may take $\gamma_{13} = \gamma_{23} = \Gamma/2$, where Γ is the excited state spontaneous emission rate. Including these exponential dephasing terms in Eqns. 9 we obtain

$$\begin{aligned} \dot{\rho}_{13} &= i(\Delta_p + i\gamma_{13}) \rho_{13} - i\chi_c^* \rho_{12} - i\chi_p^* \\ \dot{\rho}_{12} &= i(\Delta_p - \Delta_c + i\gamma_{12}) \rho_{12} - i\chi_c \rho_{13} \end{aligned} \quad (10)$$

Experiments deal with real atoms that have multiple levels - a limitation of our three-level model is that we consider a “closed” system where we do not account for population leaking to extraneous energy-levels. Even so, the three-level model is widely-used and predicts experimental outcomes, at least qualitatively, surprisingly well.

The most important solutions to Eqns. 10 are “steady-state solutions”, obtained for times $t \gg 1/\gamma_{12}, 1/\gamma_{13}$. In this long-time limit, at times long after the atomic variables have “relaxed” to their steady-state values, ρ_{12} and ρ_{13} are no longer functions of time. Setting $\dot{\rho}_{12}$ and $\dot{\rho}_{13}$ equal to zero, we obtain the steady-state solution:

$$\rho_{13} = \frac{\chi_p^*(\Delta_p - \Delta_c + i\gamma_{12})}{(\Delta_p - \Delta_c + i\gamma_{12})(\Delta_p + i\gamma_{13}) - |\chi_c|^2}. \quad (11)$$

Eqns. 10 and 11 are derived in Ref. [1], except that our equations include nonzero pump detuning Δ_c .

Recall from Eqn. 8 that ρ_{13} is related to the steady-state magnitude of the induced dipole moment at the probe frequency. Hence ρ_{13} has a direct connection to the polarizability of the medium (defined as the induced dipole moment per atom, which we denote by α_p). In the lab, however, we measure probe absorption. Therefore, we need to connect ρ_{13} with probe absorption. For the benefit of undergraduates who may not have had a course in optics, we briefly describe in the next subsection how we arrive at a well-known relation between the absorption and the polarizability α_p .

D. Absorption, refractive index, polarizability

The absorption and polarizability are related to each other through their connection with the refractive index. We first examine the relation between absorption and refractive index. The simplest description of the attenuation of a light beam as it propagates through a medium (say, a plane wave $\vec{E}(z, t) = \vec{E}_0 e^{i(kz - \omega t)}$ propagating in the z -direction) is given by Beer’s Law: $I(z) = I_0 \exp(-\alpha z)$, where I_0 is the intensity at $z = 0$, and α is the attenuation coefficient. The incident intensity attenuates exponentially due to both scattering and absorption - the latter dominates at near-resonance incident frequencies, in which case we may simply refer

to α as the absorption coefficient. The refractive index of the medium n enters through the well-known wave relation $k = n\omega/c$ between the spatial frequency k and temporal frequency ω . In the presence of absorption n becomes complex and we may write the refractive index in terms of real and imaginary parts: $n = n_r + in_i$. Substituting the resulting complex expression for k into the plane wave amplitude above, we find $\vec{E}(z, t) = \vec{E}_0 e^{-n_i \omega z/c} e^{i(n_r \omega z/c - \omega t)}$, from which we may derive $I(z) = I_0 \exp(-2n_i \omega z/c)$. Comparing this relation with the above mentioned statement of Beer's Law we arrive at the well-known relation between the absorption coefficient and the imaginary refractive index:

$$\alpha = 2n_i \omega/c. \quad (12)$$

Next, we remind the reader of the well-known relation between the macroscopic refractive index and the polarizability, derived by applying Maxwell's equations in a linear non-magnetic medium with no free currents:

$$n = \sqrt{1 + N\alpha_p/\epsilon_0} \xrightarrow[n \sim 1]{\text{gas}} 1 + N\alpha_p/2\epsilon_0 \quad (13)$$

Eqn. 13 is arrived at by starting with one of the curl equations, say, $\vec{\nabla} \times \vec{B} = \mu_0 \partial_t (\epsilon_0 \vec{E} + \vec{P})$, where $\partial_t \equiv \partial/\partial t$ and \vec{P} is the electric polarization of the medium (defined as the dipole moment per unit volume), i.e., $\vec{P} = N\alpha_p \vec{E}$ where N is the atomic density, or more precisely, the number of atomic dipoles per unit volume. Taking the curl on both sides of this Maxwell's equation we obtain $\nabla^2 \vec{E} = \mu_0 \epsilon_0 (1 + N\alpha_p/\epsilon_0) \partial_t^2 \vec{E}$ which, upon comparison with the wave equation $\nabla^2 \vec{E} = (n^2/c^2) \partial_t^2 \vec{E}$, yields the relation $n^2 = 1 + N\alpha_p/\epsilon_0$. For a gas the refractive index $n \sim 1$, and we may apply a binomial approximation to eliminate the square root (see Eqn. 13).

Now, how to calculate the polarizability α_p ? The answer lies in an examination of Eqns. 8 and 11 and the realization that the definition of the polarizability stated in the caption to Fig. 1 allows us to use Eqn. 3 to write:

$$\langle \hat{d} \rangle_{\text{probe}} = \alpha_p \left(\frac{1}{2} \vec{e}_p E_p e^{-i\omega_p t} + c.c. \right). \quad (14)$$

Equating terms oscillating at the same frequency in Eqns. 8 and 14, we find

$$\frac{1}{2} \alpha_p \vec{e}_p E_p = \rho_{31} \vec{d}_{13} \quad (15)$$

which, upon taking the dot product with \vec{e}_p^* on both sides and using the fact that $\vec{e}_p \cdot \vec{e}_p^* = 1$, yields

$$\frac{1}{2} \alpha_p E_p = \rho_{31} \vec{d}_{13} \cdot \vec{e}_p^* \quad (16)$$

Substituting the complex conjugate of Eqn. 11 in Eqn. 16 we obtain

$$\alpha_p = \frac{|\mu_{13}|^2}{\hbar} \frac{\Delta_p - \Delta_c - i\gamma_{12}}{(\Delta_p - \Delta_c - i\gamma_{12})(\Delta_p - i\gamma_{13}) - |\chi_c|^2} \quad (17)$$

where we have used the definition of χ_p as stated immediately after Eqn. 6, and we have introduced the symbol $\mu_{13} = \vec{d}_{13} \cdot \vec{e}_p^*$ to denote the projection of the transition dipole moment on the direction of the field polarization (note that $|\mu_{13}|^2$ is directly related to the Clebsch-Gordan coefficient for the probe transition).

We now substitute Eqn. 17 in Eqn. 13. We rationalize the expression for α_p in Eqn. 17, and equate the real and imaginary parts separately in Eqn. 13. Using Eqn. 12, we obtain for the absorption coefficient α :

$$\begin{aligned} \alpha &= \frac{N\omega_p |\mu_{13}|^2}{\epsilon_0 c \hbar} \\ &\times \frac{\gamma_{13} \Delta'^2 + \gamma_{12}(\gamma_{12}\gamma_{13} + |\chi_c|^2)}{[\Delta_p \Delta' - \gamma_{12}\gamma_{13} - |\chi_c|^2]^2 + [\gamma_{12}\Delta_p + \gamma_{13}\Delta']^2} \end{aligned} \quad (18)$$

and for the real part of the refractive index n_r

$$\begin{aligned} n_r &= 1 + \frac{N |\mu_{13}|^2}{2\epsilon_0 \hbar} \\ &\times \frac{\Delta'(\Delta' \Delta_p - |\chi_c|^2) + \gamma_{12}^2 \Delta_p}{[\Delta_p \Delta' - \gamma_{12}\gamma_{13} - |\chi_c|^2]^2 + [\gamma_{12}\Delta_p + \gamma_{13}\Delta']^2} \end{aligned} \quad (19)$$

where $\Delta' \equiv$ relative probe-coupling detuning $\Delta_p - \Delta_c$ (also referred to as the Raman detuning).

It is instructive to examine Eqns. 18 and 19 in the limit $\chi_c = 0$ (pump off). Of course, no EIT occurs so we should recover the usual results for absorption and real refractive index. Eqn. 18 for the absorption yields

$$\alpha \xrightarrow{\chi_c=0} \frac{N\omega_p |\mu_{13}|^2}{\epsilon_0 c \hbar} \frac{\gamma_{13}}{\Delta_p^2 + \gamma_{13}^2} \quad (20)$$

which follows the expected Lorentzian absorptive line shape with half width at half maximum (HWHM) γ_{13} for a stationary atom, attaining its maximum value at $\Delta_p = 0$. Eqn. 20 is depicted in Fig. 2(a) for the ^{87}Rb D1 transition where $2\gamma_{13}/2\pi = 5.75$ MHz [5].

For the real refractive index we find from Eqn. 19,

$$n_r \xrightarrow{\chi_c=0} 1 + \frac{N |\mu_{13}|^2}{2\epsilon_0 \hbar} \frac{\Delta_p}{\Delta_p^2 + \gamma_{13}^2} \quad (21)$$

which yields the usual dispersive line shape around probe-resonance, again with a HWHM of γ_{13} . Eqn. 21 is depicted in Fig. 2(c).

Recall from Sec. 1B that Δ_p is defined to be positive when the probe is detuned below resonance, and negative above. The decrease in n_r with frequency near resonance, seen in Fig. 2 (c), is the well-known "anomalous refractive index" effect, anomalous because as one may recall from the classic experiment of passing white light through a glass prism, red light deviates the least and blue the most, signifying that in the usual case (i.e., far from resonance) n_r increases with frequency.

E. EIT contrast and line width

When the control field is on ($\chi_c \neq 0$), the absorption α in Eqn. 18 takes the form as plotted in Fig. 2(b). EIT

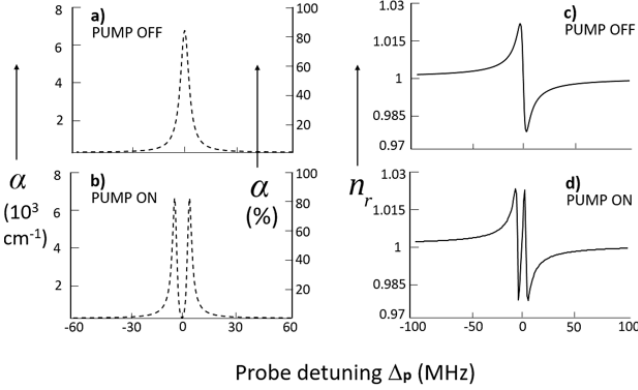


Fig. 2. The absorption coefficient α , depicted by the dashed lines in (a) and (b), and the real refractive index n_r , depicted by the solid lines in (c) and (d), as predicted by Eqns. 18-21. The case of “no pump” ($\chi_c = 0$) is shown in the top panel (Eqns. 20 and 21) as compared to the “EIT case” ($\chi_c \neq 0$) which is shown in the bottom panel (Eqns. 18 and 19). We used plot parameter-values close to conditions in our experiments: For the ^{87}Rb D1 transition $\gamma_{13}/2\pi = \frac{1}{2}(5.75 \text{ MHz})$, and $\gamma_{12}/2\pi = 3 \text{ kHz}$; $|\chi_c|/2\pi = 4 \text{ MHz}$, $\omega_p/2\pi = 3.77 \times 10^{14} \text{ Hz}$, $N = 3.36 \times 10^{11}/\text{cm}^3$, $|\mu_{13}| = 2.54 \times 10^{-29} \text{ Cm}$, $\Delta_c = 0$.

manifests as a dramatic drop in absorption when the coupling and probe beams are in resonance with each other. In order to obtain simplified expressions for the contrast and line width of the EIT transmission window, we set the probe detuning Δ_p equal to zero in Eqn. 18:

$$\alpha \xrightarrow{\Delta_p=0} \alpha_{\chi_c=0} \left[1 - \frac{|\chi_c|^2}{\gamma_{13}} \frac{\gamma_{12} + \frac{|\chi_c|^2}{\gamma_{13}}}{\Delta_c^2 + \left(\gamma_{12} + \frac{|\chi_c|^2}{\gamma_{13}} \right)^2} \right] \quad (22)$$

where $\alpha_{\chi_c=0}$ is obtained by plugging $\Delta_p = 0$ in Eqn. 20. The first term inside the parentheses in Eqn. 22 represents the baseline absorption without EIT, while the second term is the EIT transmission window - the dip in absorption depicted in Fig. 2(b). This dip in absorption is Lorentzian with a full-width-half-maximum given by:

$$\Gamma_{EIT} = 2 \left(\gamma_{12} + \frac{|\chi_c|^2}{\gamma_{13}} \right) \quad (23)$$

The EIT contrast, or amplitude of the transparency window, is denoted by Δa and is simply obtained by setting $\Delta_c = 0$ in the second term of Eqn. 22:

$$\Delta a = \frac{|\chi_c|^2}{\gamma_{13}\gamma_{12} + |\chi_c|^2} \quad (24)$$

However, as explained in the main article, the closed three-level expressions in Eqns. 18 - 24 above, while useful for visualizing the dependence of the EIT linewidth and contrast on various parameters (see Fig. 2), are not useful for making quantitative predictions of the linewidth and contrast actually observed in experiments.

F. Dark and bright states in EIT

In order to better understand the results in Sec. 1 E above, we ask the question: What are the new eigenstates and eigenenergies for the Hamiltonian in Eqn. 1 describing the three-level atomic system in Fig. 1(a) under illumination by the coupling and probe fields?

To address this question it is advantageous to know the Hamiltonian in matrix form, under the rotating wave approximation and long wavelength approximation, denoted here by \hat{H}_{RWA} . In order to do this using the optical Bloch equations already derived in Sec. 1 C we begin by casting the Schrodinger equation (Eqn. 1) in terms of the density matrix $\hat{\rho}$. We have

$$i\hbar\dot{\hat{\rho}} = \left[\hat{H}_{RWA}, \hat{\rho} \right], \quad (25)$$

where $\hat{\rho}$ and \hat{H}_{RWA} are Hermitian matrices, of order 3×3 for the three-level system, each with nine matrix elements of the form ρ_{ij} and H_{ij} (where $i, j = 1, 2, 3$). For the purpose of this sub-section it is convenient to ignore all damping and decoherence processes such as spontaneous emission, collisions, etc. From Eqn. 9 we see that we know all the matrix elements for $\dot{\hat{\rho}}$ already, and can use them to re-construct the Hamiltonian \hat{H}_{RWA} . For example, from Eqn. 25, the matrix elements $i\hbar\rho_{12}$ and $i\hbar\rho_{13}$ are, respectively,

$$\begin{aligned} \left[\hat{H}_{RWA}, \hat{\rho} \right]_{12} &= -H_{22}\rho_{12} - H_{12} - H_{32}\rho_{13} \\ \left[\hat{H}_{RWA}, \hat{\rho} \right]_{13} &= -H_{33}\rho_{13} - H_{13} - H_{23}\rho_{12} \end{aligned} \quad (26)$$

where we have used the weak-probe approximation $\rho_{32} \approx 0$, $\rho_{22} \approx 0$, and $\rho_{11} \approx 1$ as discussed earlier in Sec. 1C, and we also used $H_{11} = 0$. Comparing the coefficients of the ρ_{12} and ρ_{13} terms in Eqns. 26 and 9, we find

$$H_{RWA} = \hbar \begin{bmatrix} 0 & 0 & -\chi_p^* \\ 0 & -(\Delta_c - \Delta_p) & -\chi_c^* \\ -\chi_p & -\chi_c & \Delta_p \end{bmatrix} \quad (27)$$

Setting the pump and probe detunings equal to zero for simplicity, we find the three eigenvalues for the Hamiltonian in Eqn. 27 to be:

$$(\lambda_0, \lambda_{\pm}) = (0, \pm\hbar\Omega) \quad (28)$$

where Ω is a generalized Rabi frequency defined in terms of the sum of the squares of the pump and probe Rabi frequencies: $\Omega \equiv \sqrt{|\chi_c|^2 + |\chi_p|^2}$. The three orthonormal eigenstates corresponding to these eigenvalues are:

$$\begin{aligned} |0\rangle &= \frac{1}{\Omega} (\chi_c|1\rangle - \chi_p|2\rangle) \\ |\pm\rangle &= \frac{1}{\sqrt{2}} \left(\frac{\chi_p^*|1\rangle + \chi_c^*|2\rangle}{\Omega} \mp |3\rangle \right) \end{aligned} \quad (29)$$

Two revealing insights are obtained from Eqns. 29. First, an atom that happens to be in eigenstate $|0\rangle$ has no overlap with state $|3\rangle$, hence can never excite into

state $|3\rangle$. For this reason we refer to $|0\rangle$ as a *dark state*. Note that, in the weak probe approximation ($\chi_p \ll \chi_c$) we find that $|0\rangle \approx |1\rangle$. Second, if we re-cast the two non-dark states $|\pm\rangle$ in Eqn. 29 in terms of two new *non-stationary* states $|+\rangle'$ and $|-\rangle'$:

$$|\pm'\rangle = \frac{1}{\sqrt{2}} (|-\rangle \pm |+)\quad (30)$$

we see that, in the weak probe approximation, $|+\rangle' \approx |2\rangle$ and $|-\rangle' \approx |3\rangle$. Here, $|+\rangle'$ and $|-\rangle'$ are not stationary states because the strong coupling field oscillates the atoms back and forth between $|+\rangle' \approx |2\rangle$ and $|-\rangle' \approx |3\rangle$. We therefore refer to the $|+\rangle'$ -state, which is strongly coupled to $|3\rangle$, as the *bright state*. Thus, the corollary is that in the weak probe approximation, we may think of states $|1\rangle$ and $|2\rangle$ in our three-level system (see Fig. 1(a)) as the dark state and bright state, respectively.

Note that atoms in the bright state soon get optically pumped into the dark state where they stay. However, as indicated in the main article, our simple “closed” three-level model for a single atom does not adequately replicate the dense samples of moving atoms with multiple levels that are used in our experiments, and this transfer to the dark state is reduced, leading to significantly reduced EIT contrast.

G. Slow light

The entire discussion in Sec. 1 E above was centered around probe absorption α (Eqn. 18) in the presence of a coupling field - in this sub-section we focus on the real refractive index n_r (Eqn. 19) which is plotted in Fig. 2(d). Slow light arises from the dramatic change in refractive index n_r within the narrow EIT transparency window where the coupling (i.e., pump) and probe beams are in resonance with each other.

The steep gradient of n_r at zero pump-probe detuning significantly impacts the group velocity of light v_g :

$$v_g(\omega_p) \equiv \frac{c}{n_r + \omega_p d n_r / d \omega_p} \quad (31)$$

In particular a steep *positive* gradient about zero detuning, as depicted in Fig. 2, leads to a significantly reduced group velocity. This is elucidated by putting $\Delta_c = 0$ for simplicity in Eqn. 19 and considering the case of strong coupling intensity, i.e.,

$$|\chi_c|^2 \gg \Delta_p^2, \gamma_{12}^2, \gamma_{12}\gamma_{13}, |\Delta_p|\gamma_{13}, \quad (32)$$

to find

$$n_r = 1 - \frac{N}{2\epsilon_0\hbar} \frac{|\mu_{13}|^2}{|\chi_c|^2} \Delta_p. \quad (33)$$

Substituting Eqn. 33 in Eqn. 31, and recalling that $\Delta_p \equiv \omega_{31} - \omega_p$, we obtain for the group velocity

$$\frac{v_g}{c} \approx \frac{|\chi_c|^2}{|\chi_c|^2 + \frac{N|\mu_{13}|^2}{2\epsilon_0\hbar}\omega_p}. \quad (34)$$

If we choose the coupling intensity such that we satisfy:

$$|\chi_c|^2 \ll \frac{N|\mu_{13}|^2}{2\epsilon_0\hbar} \omega_p \quad (35)$$

we can make $v_g/c \ll 1$, thus achieving slow light.

As explained in the main article, the conditions in Eqns. 32 and 35 are always satisfied in our experiments.

2. Rubidium hyperfine structure

Our experiments are performed on the D1 transition $5^2S_{1/2}, F_g = 2 \rightarrow 5^2P_{1/2}, F_e = 1$ in ^{87}Rb atomic gas. Among the alkali elements Rubidium is popular owing to the ready availability of inexpensive user-friendly commercial diode lasers at the resonance wavelength for transitions from the $5^2S_{1/2}$ ground state to either the $5^2P_{1/2}$ excited state (D1-transition; 795 nm) or the $5^2P_{3/2}$ excited state (D2-transition; 780 nm). Fig. 3 shows hyperfine energy-levels for both stable isotopes ^{85}Rb (nuclear spin $I = 5/2$) and ^{87}Rb ($I = 7/2$) [5].

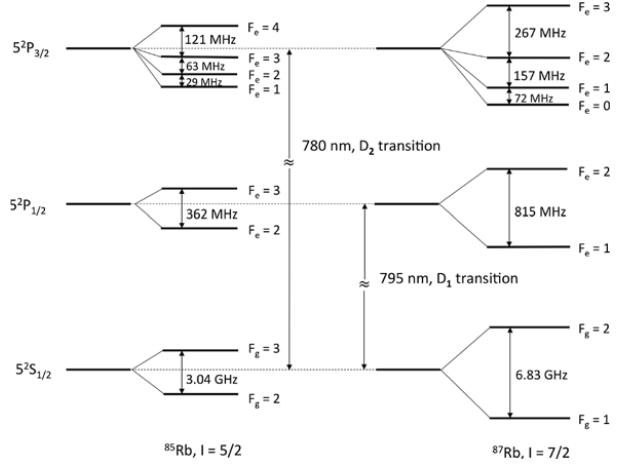


Fig. 3. Rb energy-levels. When we account for electron spin-orbit interaction, the hydrogenic states $5S$ and $5P$ are converted to $5S_{1/2}$ and $5P_{1/2}, 5P_{3/2}$ energy-levels - this is the *fine structure*. The interaction between electron angular momentum and nuclear spin yields the *hyperfine structure*, denoted by the F -quantum numbers. A weak magnetic field causes Zeeman splitting of each of these F -levels into $2m_F + 1$ magnetic sub-levels with quantum numbers $-m_F, -m_F + 1, \dots, m_F - 1, m_F$ (not shown).

As shown in Fig. 3, the hyperfine D1 structure for ^{87}Rb consists of the $5^2S_{1/2}$ ground state and the $5^2P_{1/2}$ excited state, which are split by the interaction of the valence electron’s total angular momentum (orbital + spin) with the nuclear spin, creating $F_g = 1, 2$ ground energy states (separated by 6.8 GHz), and $F_e = 1, 2$ excited energy states (separated by 815 MHz), respectively. Each hyperfine state F has $2F + 1$ degenerate substates with quantum number m ranging from $m = -F$ to F in increments of 1. A measurement will find the atom to have an angular momentum component $m\hbar$ along any

chosen quantization axis - we choose the z -axis as our axis of quantization. For, say the $F_g = 2$ ground state, the five magnetic substates are revealed in the presence of a weak external magnetic field B_z along the z -axis which removes the degeneracy by imparting the well-known Zeeman shift: $\Delta E = g_f \mu_B m_{F_g} B_z$ to each magnetic sub-level, where g_f is the Lande g-factor for the atomic hyperfine state (1/2 for the $F_g = 2$ ground state), μ_B is the Bohr magneton (9.274×10^{-28} Joules/Gauss), B_z is the external magnetic field magnitude in Gauss and m_{F_g} is the magnetic sub-level number. The Zeeman shifts between the magnetic sub-levels of the $F_g = 2$ ground state are 0.7 KHz/mG [5].

3. Suppression of stray magnetic fields

In this section we describe in detail how to suppress below 0.2 mG any stray magnetic fields in the laser-atom interaction region. The mu-metal shields need to be frequently de-gaussed using a procedure described below. Further, we describe below a reliable accurate method that is needed to measure the total stray residual magnetic field at levels well below 0.5 mG (less than 1% of the Zeeman field B_z) in the laser-atom interaction region. Typical high-end commercial gauss meters are reliable for measuring magnetic fields down to 10-20 mG, but not below.

A. Degaussing the magnetic shields

The mu-metal sheets lose shielding effectiveness over a period of a few days, primarily owing to mechanical stress created by removing and replacing the end-caps on the triple-shield in order to make changes in the optical setup inside. This is attributed to atomic dipoles becoming progressively magnetically locked together through their own interactions rather than external fields. Therefore, we degaussed the shields just before taking data.

In order to degauss the shields we subject the mu-metal to a large AC magnetic field and slowly lower the strength down to zero. The large AC field will overcome the locked dipoles, forcing their alignment with the AC field. In our experiments, we use a cable wound around the layer of thermal foam (see Fig. 5 in main article) surrounding the inner most mu metal shield to supply the degaussing current. There are ~ 80 turns over a length of ~ 20 cm.

The appropriate rate of decreasing the current is determined empirically. If not decreased optimally, residual fields continue to circulate in the innermost shield which can be detected, as discussed in Sec. 3 B below. By repeatedly modifying and iterating the degaussing process to optimally suppress the residual field we determined an adequate degaussing procedure: We passed a peak current of 5 A through the cable which is slowly lowered over 1-2 minutes using a variac; the current is reduced twice as slowly when under 200 mA.

B. Residual magnetic field measurements

In this sub-section we discuss how to measure residual stray magnetic fields in the entire laser-atom interaction volume - a cylinder of diameter equal to that of the probe beam and length equal to that of the vapor cell - by using a dedicated auxiliary optical pumping technique [6]. We reduce the total stray residual magnetic field well below 0.5 mG (less than 1% of the Zeeman field B_z) as shown below.

To elucidate slow light investigations based on Zeeman EIT we rely upon a well-defined quantization axis (the z -axis), which in our case is collinear with the weak external constant magnetic field B_z and the propagation direction of the pump and probe laser beams. B_z creates Zeeman sub-levels, for each of which the magnetic dipole moment precesses around B_z with an angular momentum component $m\hbar$ along the z -axis. For this choice of quantization axis, if the electric field vector of the incident light field is perpendicular to the z -axis, as is the case for our pump and probe beams, the induced (i.e., absorptive and stimulated) transitions among the Zeeman sub-levels obey the selection rule $\Delta m = \pm 1$ [7]. In other words, the absorption depends upon the projections of the precessing magnetic dipoles along the z -axis. Spontaneous emission from the excited Zeeman states is not associated with any special quantization axis and is constrained only by the selection rule $\Delta m = 0, \pm 1$.

Therefore, any small departure from collinearity between the laser propagation direction and the applied longitudinal magnetic field results in a small component of the strong pump beam (and the weak probe beam too, which we may neglect compared to the pump) causing a persistent undesired $\Delta m = 0$ cycling of some atoms between the $m_{F_g} = 1$ and $m_{F_e} = 1$ levels in Fig. 3(b) in the main article. This weakens our approximation to a three-level lambda scheme, decreasing EIT contrast and broadening EIT linewidth, thus significantly reducing slow light effects.

Assuming the presence of a residual magnetic field pointing along some arbitrary direction, and setting the solenoid current equal to zero, we illuminate the atoms with a single strong circularly-polarized beam, say a σ^+ beam in Fig. 3(b) in the main article, propagating along the z -direction (still the quantization axis), tuned to the $F_g = 2 \rightarrow F_e = 1$ transition. The σ^+ beam intensity I is strong enough ($I > I_{sat}$), and illuminates the atoms for long enough, that a substantial number of atoms is optically pumped into the $F_g = 2, m_{F_g} = +1, +2$ magnetic sub-levels. Turning the strong laser beam off at this point allows the “spin polarization” of the sample to decay, until the population is distributed evenly among the $F_g = 2$ magnetic sub-levels. Note that the transition strengths are different for each specific Δm -transition. Thus sample absorption changes appreciably as the spin polarization decays from strongly polarized to unpolarized.

However, during this depolarization process, the presence of a weak non-axial magnetic field means that the

total magnetic field \vec{B} is not aligned with the z -axis. The atomic magnetic dipoles precess around \vec{B} at the Larmor frequency ν_L , given by $h\nu_L = g_f\mu_B|\vec{B}|$. The constants g_f and μ_B are the Lande g-factor and Bohr magneton, respectively, and are provided in Sec. 1 above. The projections on the z -axis of the magnetic dipoles precessing around \vec{B} oscillate at the Larmor frequency, leading to observable oscillations in the sample absorption at ν_L . By measuring the oscillation frequency of spin depolarization with a weak σ^+ probe beam ($I \ll I_{sat}$), we can determine the magnitude of the weak stray B -field from the expression for the Larmor frequency above.

To perform this measurement with best signal-to-noise ratio we create as many spin-polarized atoms as possible by using the vapor cell with higher buffer gas pressure (30 Torr) mentioned in Sec. 5B of the main article, warmed to 65°C to push the number density up to $3.8 \times 10^{11}/\text{cm}^3$ (see Fig. 7(a) in the main article). As outlined in Sec. 3B of the main article, the buffer gas helps suppress rapid spin depolarization due to collisions and transit time effects. We illuminate the atoms with a single circularly polarized beam for which the intensity is square-wave-modulated between two states: A high-intensity state (the pump phase), in which the beam is intense (4.3 mW/cm² in our case) for a period of 500 ms, followed by a low-intensity state (the probe phase) where the beam intensity is kept at 0.044 mW/cm². The low-intensity state is 500 ms long too, though only the first 50 ms need to be recorded. The switching-time between the two intensity-states is 15 μs . Clear oscillations in the absorption are visible, as shown in Fig. 4(a) for the case of a residual stray magnetic field of 139 μG .

Fig. 4(b) shows that the application of a small axial magnetic field (here, $B_z = 2.4$ mG) suffices to cause the

magnetic dipoles to precess around the z -axis, in which case the projection of each dipole moment along the z -axis ceases to oscillate. The sample is optically pumped toward the $F_g = 2, m_{F_g} = +1, +2$ magnetic sub-levels by the σ^+ -pump, therefore the absorption smoothly increases as the sample becomes spin-polarized.

The inset in Fig. 4(a) shows that this stray B -field measurement technique can be used to optimize the mu-metal shield degaussing procedure. In the example shown, persistent currents in the innermost shield lead to detectable Larmor oscillations in the absorption, corresponding to a residual non-axial magnetic field nearly twice the strength of the typical case depicted in the main plot in Fig. 4(a).

References

1. P. W. Milonni and J. H. Eberly, “Laser Physics”, Wiley (2010), Sec. 9.10, pp 441 - 446
2. This can be seen by considering the Lorentz force in Gaussian units: $\vec{F} = e(\vec{E} + \vec{v}/c \times \vec{B})$, where \vec{E} and \vec{B} have the same dimensions. The second term is negligible when $v \ll c$.
3. For a spatially extended sample illuminated by a *plane* electromagnetic wave propagating in the z -direction, the field $\hat{\vec{E}}$ incident on an atom located at z has a spatial phase e^{ikz} . This spatial phase can be included in the Rabi frequency which is defined immediately after Eqn. 6. However, note that the result for the polarizability α_p in Eqn. 17 depends only on $|\chi_c|^2$, i.e., α_p is the same for all the atoms in the sample. Hence, it is justified to use Eqn. 17 in the macroscopic expression Eqn. 13 in order to obtain Eqns. 18 and 19.
4. See Sec. 9.4 in Ref. [1] for a nice description of how to include relaxation processes in the density matrix.
5. <https://steck.us/alkalidata/>, “Rubidium 85 D line data” and “Rubidium 87 D line data”, by Daniel Steck, University of Oregon
6. M. Shuker, “Decay processes in EIT medium”, PhD thesis, Technion - Israel Institute of Technology (2008)
7. On the other hand, if the electric field vector of the incident light field is along the z -axis, the induced transitions among the Zeeman sub-levels obey the selection rule $\Delta m = 0$, even though the pump and probe beams are ostensibly prepared in Sec. 4B of the main article as σ^+ and σ^- beams.

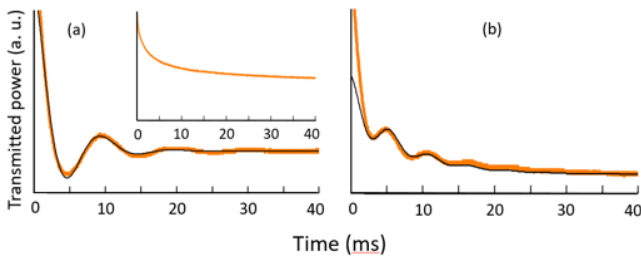


Fig. 4. a) Setting the solenoid current to zero, we can measure the total stray magnetic field by observation of oscillations in the absorption at the Larmor precession frequency, which is determined by fitting with a decaying oscillatory function. Using the equation connecting Larmor frequency to magnetic field (see text), we find a total stray field of 139 μG in a typical measurement. The inset shows that by turning on a small solenoid current, the application of a small axial magnetic field, 2.4 mG in this case, is sufficient to cause the Larmor oscillations in absorption to disappear. b) If the de-gaussing procedure is not optimized, the same measurement typically yields a significantly higher stray residual magnetic field, 244 μG in this case.